

# An X-ray Detected Group of Quiescent Early-type Galaxies at $z = 1.6$ in the Chandra Deep Field South

Masayuki TANAKA<sup>1</sup>, Alexis FINOGUENOV<sup>2,3</sup>, Mohammad MIRKAZEMI<sup>2</sup>, David J. WILMAN<sup>2</sup>, John S. MULCHAEY<sup>4</sup>, Yoshihiro UEDA<sup>5</sup>, Yongquan XUE<sup>6,7,8</sup>, William N. BRANDT<sup>6,7</sup>, Nico CAPPELLUTI<sup>9</sup>

<sup>1</sup>*Institute for the Physics and Mathematics of the Universe, The University of Tokyo, 5-1-5 Kashiwanoha, Kashiwa-shi, Chiba 277-8583, Japan*

<sup>2</sup>*Max-Planck Institut für extraterrestrische Physik, Giessenbachstrasse, D-85748 Garching bei München, Germany*

<sup>3</sup>*University of Maryland, Baltimore County, 1000 Hilltop Circle, Baltimore, MD 21250, USA*

<sup>4</sup>*The Observatories of the Carnegie Institution of Science, 813 Santa Barbara Street, Pasadena, CA 91101, USA*

<sup>5</sup>*Department of Astronomy, Kyoto University, Kyoto 606-8502, Japan*

<sup>6</sup>*Department of Astronomy and Astrophysics, Pennsylvania State University, University Park, PA 16802, USA*

<sup>7</sup>*Institute for Gravitation and the Cosmos, Pennsylvania State University, University Park, PA 16802, USA*

<sup>8</sup>*Key Laboratory for Research in Galaxies and Cosmology, Department of Astronomy, University of Science and Technology of China, Chinese Academy of Sciences, Hefei, Anhui 230026, China*

<sup>9</sup>*INAF-Osservatorio Astronomico di Bologna, Via Ranzani 1, 40127 Bologna, Italy*

(Received ; accepted )

## Abstract

We report the discovery of an X-ray group of galaxies located at a high redshift of  $z = 1.61$  in the Chandra Deep Field South. Based on the 4Msec Chandra data, the group is first identified as an extended X-ray source. We use a wealth of deep multi-wavelength data to identify the optical counterpart – our red sequence finder detects a significant over-density of galaxies at  $z \sim 1.6$ . The brightest group galaxy is spectroscopically confirmed at  $z = 1.61$  based on published spectroscopic redshifts. Using this as a central redshift of the group, we measure an X-ray luminosity of  $L_{0.1-2.4\text{keV}} = (1.8 \pm 0.6) \times 10^{43} \text{ erg s}^{-1}$ , which then translates into a group mass of  $(3.2 \pm 0.8) \times 10^{13} M_{\odot}$ . This is the lowest mass group ever confirmed at  $z > 1.5$ . The deep optical-nearIR images from CANDELS reveal that the group exhibits a surprisingly prominent red sequence and most of the galaxies are consistent with a formation redshift of  $z_f = 3$ . A detailed analysis of the spectral energy distributions of the group member candidates confirms that most of them are indeed passive galaxies. Furthermore, their structural parameters measured from the near-IR CANDELS images show that they are morphologically early-type. The newly identified group at  $z = 1.61$  is dominated by quiescent early-type galaxies and the group appears similar to those in the local Universe. One possible difference is the high fraction of AGN —  $38^{+23}_{-20}\%$  of the bright group member candidates are AGN, which might indicate a role for AGN in quenching of star formation. However, a statistical sample of high- $z$  groups is needed to draw a general picture of groups at this redshift. Such a sample will hopefully be available in near future surveys.

**Key words:** galaxies:clusters: individual: CL J033211.67-274633.8 — galaxies: formation — galaxies: evolution — galaxies: fundamental parameters

## 1. Introduction

Modern observing facilities can reach galaxy groups and clusters at  $z = 1.5$  and beyond. The number of such high- $z$  systems has been increasing in recent years and we are now in the process of building a statistical sample which will give us a detailed picture of group/cluster evolution at high redshifts. It is a widely accepted fact that galaxy clusters today are dominated by quiescent early-type galaxies, while a significant fraction of field galaxies are star forming late-type galaxies. This clearly shows that the formation and evolution of cosmic large-scale structure affects galaxy evolution. However, the interplay between galaxies and their surrounding structure remains unclear. One observational approach to this question is to study groups and clusters over a range of redshift to

directly trace their evolution and to identify the epoch when quiescent early-type galaxies become the dominant population. High- $z$  groups are statistically likely progenitors of the present-day clusters and they are thus key objects to improve our understanding of the origin of the environmental dependence observed in the local universe.

In this respect, the current frontier of high- $z$  systems is at  $z \sim 1.5$  – a number of such systems have been reported to date. Mullis et al. (2005) reported on the discovery of a rich  $z = 1.39$  cluster. It is very massive (Jee et al. 2009) and exhibits a tight red sequence (Lidman et al. 2008). Star forming galaxies are absent in the cluster core (Bauer et al. 2011). Stanford et al. (2005) discovered a cluster at  $z = 1.41$  based on infrared photometry from Spitzer. Brodwin et al. (2011) carried out a spectroscopic follow-up observation of the cluster and confirmed more

than 10 members. They also presented a spectroscopically confirmed cluster at  $z = 1.49$  selected from the Spitzer photometry. Stanford et al. (2006) presented a cluster located at  $z = 1.45$ . Follow-up spectroscopic observations and Chandra observations are reported in Hilton et al. (2007, 2010). Although exhibiting a prominent red sequence (Bielby et al. 2010), this cluster also hosts a significant number of emission line objects in the core (Hayashi et al. 2010). In the last few years, the redshift barrier of  $z = 1.5$  has been broken. Papovich et al. (2010) and Tanaka et al. (2010) independently confirmed a group at  $z = 1.62$  in the Subaru/XMM-Newton Deep Field (SXDF). Pierre et al. (2011) performed a Chandra observation of the group. Although the exposure time was rather short and the detection was marginal, they reported a consistent flux with that of Tanaka et al. (2010). The XMM-Newton Deep Cluster Project reported the discovery of a few X-ray bright clusters at  $z \sim 1.5$  (Fassbender et al. 2011; Nastasi et al. 2011; Santos et al. 2011). Even higher redshift systems are now detected. Henry et al. (2010) reported on a possible X-ray group at  $z = 1.75$  and Stanford et al. (2012) recently presented a spectroscopically confirmed X-ray cluster at  $z = 1.75$ . Gobat et al. (2011) presented a color-selected group at  $z = 2.07$ . There are a few more photo- $z$  selected group candidates at  $z \sim 2$  (Andreon et al. 2009; Spitler et al. 2011). However, some of these very high- $z$  systems still require convincing confirmation with spectroscopic redshifts.

At  $z \gtrsim 2$ , there are few securely confirmed, gravitationally bound systems but a number of authors have reported the discovery of so-called proto-clusters. The definition of a proto-cluster is often ambiguous, but here we define it as a system that exhibits a significant over-density of galaxies but is yet to be gravitationally bound. Such proto-clusters have often been identified by tracing emission line galaxies or color-selected galaxies (e.g., Venemans et al. 2002; Kurk et al. 2004; Matsuda et al. 2004; Venemans et al. 2007). Distant radio galaxies have been frequent targets for such observations (see Miley & De Breuck 2008 for a review). Some of the reported proto-clusters may collapse and evolve into a cluster at later times. These proto-clusters tend to show a significant fraction of star forming galaxies. This is at least partly due to the way they are identified, but a large population of star forming galaxies at high redshift is not unexpected. Galaxy formation occurs at density peaks – thus proto-clusters are an obvious place to find active star formation in the early universe. Clusters change their nature with time from a place for star forming galaxies to a place for quiescent, passively evolving galaxies. To identify this key, cradle-to-grave transition epoch remains an important, but as yet unfulfilled goal.

In order to address these questions, we are conducting a systematic survey of groups and clusters of galaxies using X-ray and optical-nearIR data in deep fields such as COSMOS, CFHT Deep Fields, and SXDF (Finoguenov et al. 2007; Bielby et al. 2010; Finoguenov et al. 2010). These group catalogs include systems over a wide redshift range ( $0 < z < 1.5$ ) and are a powerful probe of cosmology (e.g.,

Finoguenov et al. 2010). At the same time, they provide an ideal data set to study the evolution of galaxies across environment and time. As part of this project, we have constructed an X-ray group catalog in the Chandra Deep Field South (CDFs) as presented by Finoguenov et al. (2012 in prep). During the course of this work, we have identified a high redshift group located at  $z = 1.6$ . This system is in the large-scale structure at  $z = 1.6$  discovered by Kurk et al. (2009) and is the first gravitationally bound, X-ray detected system in that structure. It happens to fall within the area covered by the CANDELS survey (Grogin et al. 2011; Koekemoer et al. 2011), where deep, high-quality HST imaging data are available. The near-IR CANDELS images neatly probe the rest-frame optical wavelengths of galaxies at  $z = 1.6$ . We take this unique opportunity to study the galaxy population of this  $z = 1.6$  group with a depth equivalent to that typically only found at  $z = 0$ .

The layout of this paper is as follows. We review the data that we use in this work, including the creation of our X-ray group catalog in Section 2, followed by analyses of the  $z = 1.6$  group detection via extended X-ray emission and color-magnitude diagrams in Section 3. We perform a detailed analysis of spectral energy distributions (SEDs) of the group galaxies in Section 4 and examine morphology of the galaxies in Section 5. Section 6 discusses implications of our finding for the origin of the environmental dependence of galaxy properties and Section 7 concludes the paper. Unless otherwise stated, we assume a flat universe with  $H_0 = 72 \text{ km s}^{-1} \text{ km}^{-1}$ ,  $\Omega_M = 0.26$  and  $\Omega_\Lambda = 0.74$ . Magnitudes are given in the AB system. We use the following abbreviations : AGN for active galactic nucleus, BGG for brightest group galaxy, CDFS for Chandra Deep Field South, FWHM for full-width at half maximum, IMF for initial mass function, PDF for probability distribution function, PSF for point spread function, SED for spectral energy distribution, SFR for star formation rate, and SXDF for Subaru/XMM-Newton Deep Field.

## 2. Data and a Catalog of X-ray Groups in CDFS

We base our analysis on a wealth of public data available in CDFS. We first summarize the X-ray and optical-IR data that we use. We then briefly describe our X-ray group catalog.

### 2.1. X-ray data from Chandra and XMM-Newton

The Chandra Deep Field South has been a frequent target of X-ray observations with both Chandra and XMM-Newton. After the first 1Ms Chandra observation (Giacconi et al. 2002), the exposure was recently extended to 2 Ms (Luo et al. 2008; Luo et al. 2010; Rafferty et al. 2011) and later to 4Ms (Xue et al. 2011), via a large Director’s Discretionary Time project. CDFS now provides our most sensitive 0.5–8 keV view of distant AGNs, starburst galaxies, normal galaxies, and galaxy groups. For the detection of extended sources, of value is both the 3.3 Ms XMM coverage (Comastri et al. 2011) and the extended area covered by Chandra (Lehmer et al. 2005).

The group studied in this paper is detected independently in both Chandra and XMM data with a consistent source flux in the observed 0.5-2 keV band (see next section). We briefly outline the reduction of these data sets below. We note that we combine the Chandra and XMM-Newton data for the group identification in Finoguenov et al. 2012 (in prep), but we primarily use the Chandra data in this paper due to its superb spatial resolution.

In the Chandra analysis, we have applied a conservative event screening and the modeling of the quiescent background. We have filtered the light-curve events using the LC\_CLEAN tool in order to remove normally undetected particle flares. The background model maps have been evaluated with the prescription of Hickox & Markevitch (2006). We estimated the particle background by using the ACIS stowed position (<http://cxc.cfa.harvard.edu/contrib/maxim/acisbg>) observations and rescaling them by the ratio  $\frac{cts_{9,5-12keV,data}}{cts_{9,5-12keV,stowed}}$ . The cosmic background flux has been evaluated by subtracting the particle background maps from the real data and masking the area occupied by the detected sources. Rapidly broadening Chandra PSF with off-axis angle produces a large gradient in the resolved fraction of the cosmic background, which is the dominant source of systematics in our background subtraction. However, we note that the group that we study in this paper is only  $\sim 3$  arcmin away from the field center, where the Chandra PSF is still sharp. We combine the data with and without point source subtraction and analyze them independently in Sect 3.2.

For the XMM-Newton analysis, we have followed the prescription outlined in Finoguenov et al. (2007) on data screening and background evaluation, with updates described in Bielby et al. (2010). After cleaning those observations, the resulting net total observing time with XMM-Newton are 1.946Ms for pn, 2.552Ms for MOS1, 2.530Ms for MOS2. We carefully remove point sources following Finoguenov et al. (2009) and Finoguenov et al. (2010). This is done independently from the Chandra data to allow for AGN variability and difference in the astrometry. Furthermore, we do not detect individual sources and catalog them, but instead we directly work with images. This is important for XMM-Newton because it is confusion limited at the depths of CDFS (in the soft band) and the source deblending is not trivial. We are left with extended sources in the combined image. We describe the source detection in Sect 2.3 and 3.2.

## 2.2. Optical and IR data from the literature

We base our analysis mainly on two public sets of optical-IR photometry drawn from MUSIC (Grazian et al. 2006; Santini et al. 2009) and CANDLES (Grogin et al. 2011; Koekemoer et al. 2011). In addition, we make extensive use of photometric redshifts based on the deep multi-band photometry available in this field in order to identify group members.

The MUSIC catalog is a deep, multi-wavelength catalog of the CDFS field (Grazian et al. 2006; Santini et al. 2009). The catalog that we use is from Santini et al.

(2009), which is an extended version of the one presented by Grazian et al. (2006) and contains 15-band photometry spanning from the  $u$ -band to  $24\mu m$ . For details of the catalog construction, readers are referred to Grazian et al. (2006) and Santini et al. (2009). But, in short, the objects are first detected in the ACS  $z$ -band and photometry in the other bands is performed by convolving the  $z$ -band image to match with the PSF in the other bands and scaling the fluxes. Objects that are not detected in the  $z$ -band are detected and measured in the  $K_s$  and IRAC  $4.6\mu m$  images with the  $z$ -band detected objects masked out.

In addition to the MUSIC catalog, we use the deep ACS and WFC3 imaging data from CANDELS (Grogin et al. 2011; Koekemoer et al. 2011). CANDELS is a public imaging survey using the ACS and WFC3 camera on board the Hubble Space Telescope. The observation is made mainly in three bands: F814W, F125W and F160W. We make stacked F814W, F125W, and F160W images by combining data from the first 4 epochs of deep observations using the weight maps supplied by the CANDELS team. The resultant images reach limiting magnitudes of 28.3, 27.3, and 27.0 within an aperture of size  $4 \times \text{FWHM}$ . The PSF of the F160W image is  $\sim 0.2$  arcsec and the PSFs of the other images are smoothed to this size using the Gaussian kernel. Object detection and photometry is performed using Source Extractor (Bertin & Arnouts 1996). Objects are detected in the F160W image and photometry in the other bands is performed in dual image mode. We adopt MAG\_AUTO for total magnitudes and use magnitudes measured in  $4 \times \text{FWHM}$  apertures for colors. For simplicity, we often denote F814W, F125W, and F160W as  $I$ ,  $J$ , and  $H$ , respectively, in what follows. We do not make an attempt to combine the MUSIC and CANDELS catalogs because the photometry is performed in different ways and the MUSIC catalog already contains the  $i$ ,  $J$ , and  $H$ -band photometry measured in a self-consistent manner. CANDELS goes deeper than MUSIC, but most of our analyses is not limited by depth of imaging. For these reasons, we use the catalogs separately for complementary analyses.

Rafferty et al. (2011) computed photometric redshifts (photo- $z$ 's) using a combined photometric catalog collected from the literature (Wolf et al. 2004; Gawiser et al. 2006; Grazian et al. 2006; Wolf et al. 2008; Nonino et al. 2009; Taylor et al. 2009; Damen et al. 2011). They used the public photo- $z$  code ZEBRA (Feldmann et al. 2006). We note that they focused on AGNs in their paper, but they computed photo- $z$ 's for all galaxies within the extended CDFS. By comparing the photo- $z$ 's with spectroscopic redshifts, they achieved  $\sigma|\Delta z/(1+z_{spec})| = 0.03$  with an outlier rate of 4% for bright galaxies with  $R < 24$ . Here outliers are defined as those with  $|\Delta z/(1+z_{spec})| > 0.2$ . For fainter galaxies, the accuracy degrades to  $\sigma = 0.06$  and an outlier rate of 14%, although the spectroscopic sample is heterogeneous. We denote their photo- $z$ 's as  $z_{phot,rafferty}$ .

Later in the paper, we perform the spectral energy distribution (SED) fitting of group galaxies using the MUSIC catalog. The photometric redshift is fit as part of this pro-

cedure, and we shall make extensive use of these photo- $z$ 's. We denote photometric redshifts from our SED fitting as  $z_{phot,tanaka}$ . We use  $z_{phot,rafferty}$  and  $z_{phot,tanaka}$  for the selection of group members.

In addition to those sources of photometric redshift, we also examine photo- $z$ 's from Cardamone et al. (2010), which we denote  $z_{phot,cardamone}$ . Their photo- $z$ 's are based on the multi-band data from the MUSYC survey (Gawiser et al. 2006; Cardamone et al. 2010). With 18 medium-band photometry in the optical, they have achieved excellent photo- $z$ 's for bright objects (Cardamone et al. 2010). However, their broad band imaging is shallower (and covers a wider area), and the catalog is  $BVR$ -selected. This means that the fainter and redder candidate group members are not included in their catalog. For this reason, we do not use  $z_{phot,cardamone}$  for the primary selection of group members.

As each data set has its own strengths, we use different catalogs for different purposes. To be specific, the selection of the group member candidates is based on  $z_{phot,tanaka}$  and  $z_{phot,rafferty}$ . We use the CANDELS data for the color-magnitude diagrams in Section 3 because the high quality CANDELS photometry neatly probes the wavelengths around the 4000Å break. The CANDELS data are also used for structural analysis in Section 5. We base our analysis of SED fitting of the group members on the multi-band MUSIC catalog in order to cover a wide wavelength range in Section 4. We remind the readers of which photometric catalog is used at each stage of the analysis.

### 2.3. A catalog of X-ray groups in CDFS

Using the X-ray data and Rafferty et al. (2011) photo- $z$  catalog described above, we construct a catalog of X-ray groups in CDFS. We will give a full detail of the catalog construction in Finoguenov et al. (2012 in prep). But, we briefly outline our algorithm here.

On the mosaic of coadded XMM and Chandra images, group candidates are first identified as extended sources through a classical wavelet transform technique with a careful removal of point sources (Finoguenov et al. 2009). In order to identify optical counterparts of the extended X-ray emission, we apply an efficient red sequence finder as described by Finoguenov et al. (2010) and Bielby et al. (2010). The red sequence finder computes a significance of the red sequence in the region of an extended X-ray source, assuming a given redshift, by comparing observed magnitudes and colors of galaxies with a model red sequence at that redshift constructed using the recipe by Lidman et al. (2008). We achieve an efficient removal of fore-/background galaxies from the red sequence in question using the excellent photometric redshifts (Rafferty et al. 2011). Then, for each redshift at which a significant signal is detected the red sequence is visually inspected, and the group is assigned a redshift and confidence flags. We use all the public spectroscopic redshifts from the literature (Cristiani et al. 2000; Croom et al. 2001; Strolger et al. 2004; Szokoly et al. 2004; van der Wel et al. 2004; Doherty et al. 2005; Le

Fèvre et al. 2005; Mignoli et al. 2005; Ravikumar et al. 2007; Vanzella et al. 2008; Popesso et al. 2009; Balestra et al. 2010; Cooper et al. 2011) to help identify each system and obtain its spectroscopic redshift during this final step.

In total, we have spectroscopically identified 39 systems. We have another 8 systems with low quality flags. The secure groups are located mostly at  $z < 1$ , but a good fraction of them have higher redshifts. Most of the identified systems are low-mass groups with  $< 3 \times 10^{13} M_{\odot}$ . Such low-mass X-ray groups at relatively high redshift are interesting, and the unprecedented X-ray depth in the CDFS field provides an exciting opportunity to study these systems. We will discuss properties of these groups and their brightest members in Wilman et al. (in prep). The group we focus on in this paper is the spectroscopically confirmed, highest redshift group in our group catalog.

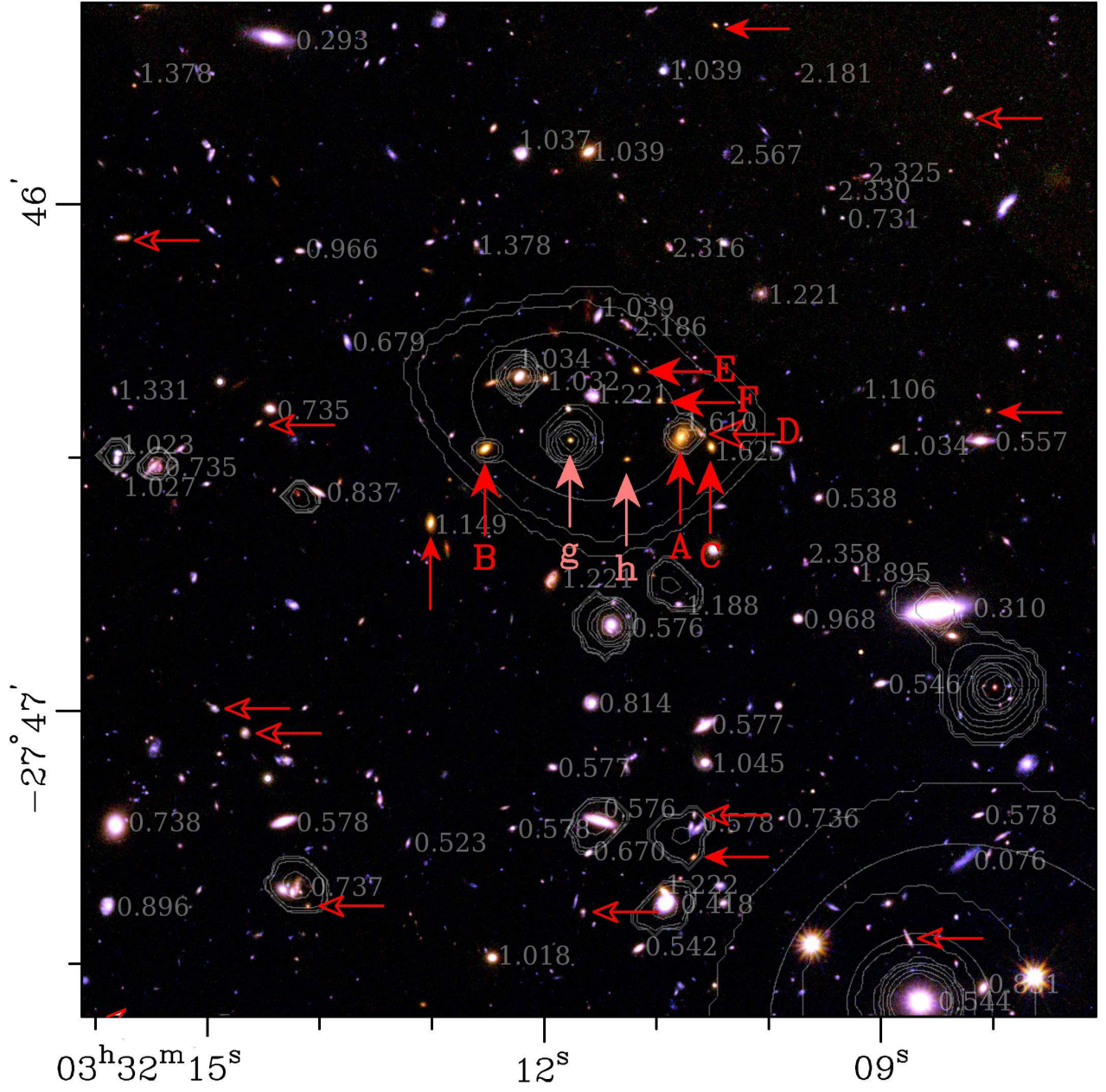
## 3. A Galaxy Group at $z = 1.6$

### 3.1. Overview of the Discovery

During the course of the group identification, we have discovered a promising high- $z$  group candidate. We have detected extended X-ray emission not far from the center of the Chandra field of view. A red sequence finder has yielded a significant signal around  $z = 1.6$  for this X-ray source. If we assume a group redshift of  $z = 1.6$ , the group has a very low X-ray luminosity, which suggests that it is a low-mass group. Such a high- $z$ , low-mass group is an interesting object because it is likely a progenitor of a present-day cluster of typical mass. For this system, a wealth of deep, multi-wavelength data are available, and furthermore, the group has recently been observed by CANDELS and the deep optical-nearIR images taken with WFC3 are publicly available. Using the CANDELS images, we present a color picture of the group in Fig. 1. In this section, we provide evidence that this system is a group located at  $z = 1.61$  with extended X-ray emission. First, we make a robust analysis of the X-ray emission and show that it is extended. We then show that there is a clear over-density of galaxies at  $z = 1.6$  around the extended X-ray emission and that the brightest group galaxy (BGG) is spectroscopically confirmed at  $z = 1.61$ . Furthermore, the galaxies form a tight red sequence, which is a ubiquitous feature of rich groups and clusters, at least at lower redshift. All of these results lead us to conclude that this system is a real group located at  $z = 1.61$ . Below, we describe each piece of evidence in detail.

### 3.2. Extended X-ray Emission from the Group

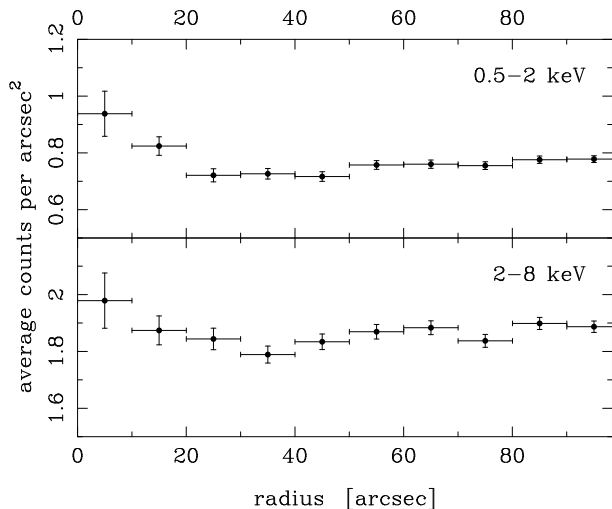
The Chandra observation reveals a number of point sources in and around the group. Together with the point sources, we detect extended, larger-scale emission around the group based on the wavelet analysis (outer contours in Fig. 1). The reader is referred to Sect. 3 of Finoguenov et al. (2007) for technical details of the wavelet analysis. The system is only  $\sim 3$  arcmin away from the center of the Chandra field of view where the PSF is very sharp and well-behaved ( $\sim 1.5$  arcsec, estimated using the profile of



**Fig. 1.** The CANDELS *IJH* pseudo-color image of the group. The contours show the X-ray emission. The arrows indicate bright ( $H < 24$ ) galaxies with  $P_{gr} \geq 0.16$  (see Section 3.3 for details). There are two types of arrow in the figure. The filled arrows point to galaxies with red colors and within  $\Delta|I - H| < 0.5$  from the model red sequence formed at  $z_f = 3$  (see Section 3.2 for details). The open arrows are bluer galaxies. The six brightest galaxies in the core of the group that have  $P_{gr} \geq 0.16$  both from Rafferty et al. (2011) and ourselves are labeled object-A to F (i.e., *good candidates*; see Section 3.2). *Likely candidates* are labeled object-g and h. The numbers show spectroscopic redshifts from the literature.

nearly point sources). As can be seen in Fig. 1, we detect the extended X-ray emission over a scale of 20 arcsec in radius, which is significantly larger than the PSF size. The extended flux is only  $3 \times 10^{-16} \text{ erg s}^{-1} \text{ cm}^{-2}$  as detailed below, but it is one of the two brightest extended objects in the Chandra best PSF area of the CDFS field ( $\lesssim 4'$  from the center). The other object is a group at  $z = 0.73$  mentioned by Cimatti et al. (2002). Extended X-ray emission can be caused by the inverse-Compton scattering of the CMB photons off energetic electrons in radio jets (e.g., Jelic et al. 2012), but there is no radio source around the X-ray emission (Miller et al. 2008). Such non-thermal origin of the X-ray emission is thus unlikely.

We perform a simple test to prove that the extended emission is real. We carry out a simple and robust analysis of counting photons around the group by masking point sources in the Chandra raw photon image. We first detect point-like objects in the image with Source Extractor (Bertin & Arnouts 1996). The detected objects are then masked out. The masking radius is set to be three times the half-width at half-maximum (HWHM), which visual inspection shows us is large enough to exclude point sources and their extended PSF wings. We have confirmed that our conclusion does not change if we change this radius to twice or four times the HWHM. We have also confirmed that our result remains the same if we use the point source catalog of Xue et al. (2011) to mask the point sources.



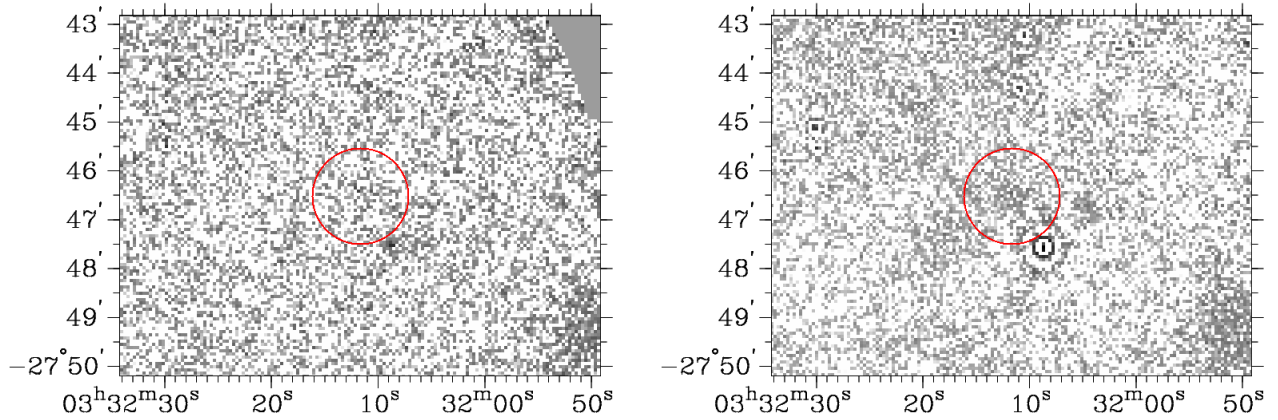
**Fig. 2.** Average photon counts per square arcsec in annuli with a width of 10 arcsec running from the center of the system to the outskirts. We here take the location of the BGG as the center. The top and bottom panels are for the soft and hard bands, respectively. Point sources are masked out and the vertical error bars show the Poisson noise.

Fig. 2 shows the average photon counts per unit area in annuli with a width of 10 arcsec for the 0.5–2 keV and 2–8 keV bands. Here, we take the BGG as the center. In the soft band, the average photon counts are clearly higher in the center and the X-ray emission is extended to 20 arcsec in radius, which is consistent with the X-ray extent from

the wavelet analysis. If we subtract the local background using the average counts from a radius of 30–60 arcsec, and interpolate over each masked area assuming the average counts within that annulus, we measure a total photon count of  $146.4 \pm 40.7$  within an aperture of 20 arcsec radius from the center (i.e.,  $3.6\sigma$  detection). If we take the center of the wavelet contours in Fig. 1 as the center, we still obtain a signal of  $3.3\sigma$ . We apply the same analysis using the 0.5–2 keV Chandra image independently reduced by Xue et al. (2011) and obtained the same result – there is a clear excess in the photon counts at the center and we measure a significant photon count from the group ( $137.6 \pm 39.5$ ). The photon count is fully consistent with ours.

The group is not detected in the hard band at a significant level as shown in Fig. 2; we measure a photon count of  $81.6 \pm 59.0$  within 20 arcsec radius after the background subtraction (i.e.,  $1.4\sigma$ ). The extended X-ray emission is therefore soft. This is consistent with the extended emission being due to intra-group medium and it rules out a significant contamination from unresolved, obscured sources. Furthermore, the flux limit for point sources in the 4Ms Chandra data at the location of the group is about  $2 \times 10^{-17} \text{ erg s}^{-1} \text{ cm}^{-2}$  in the soft band. In order to explain the X-ray flux of the group, one needs at least 15 unresolved point sources, which would correspond to an over-density of factor 30 on the scale of 15 arcsec. This is highly unlikely to happen given the clustering properties of AGNs on these scales.

Given the slightly low signal-to-noise ratio of the X-ray detection, we perform a further analysis by carefully subtracting point sources following Finoguenov et al. (2009, 2010). We present a Chandra and XMM-Newton X-ray maps Fig. 3. The X-ray emission is not readily seen by eye in the Chandra map, but this is not unexpected because the significance of the detection is not very high. From our experience, only high significance ( $> 5\sigma$ ) extended emission can be easily recognized by eye on a 2D X-ray map. If we measure the flux following Finoguenov et al. (2010), we obtain  $f_{0.5-2.0\text{keV}} = 3.1 \pm 1.0 \times 10^{-16} \text{ erg s}^{-1} \text{ cm}^{-2}$  ( $3\sigma$ ) from the Chandra image (i.e.,  $3\sigma$ ). On the other hand, the extended emission is relatively easily seen in the XMM-Newton data thanks to the larger photon collecting area. The emission is clearly extended over  $\sim 20''$  in radius, which is consistent with the wavelet detection in Fig. 1. Although we carefully removed point sources in the XMM-Newton data, one may worry about the point source contamination due to the poor spatial resolution of XMM-Newton. We argue that such contamination is likely small. We measure an X-ray flux of  $4.6 \pm 0.6 \times 10^{-16} \text{ erg s}^{-1} \text{ cm}^{-2}$  at a significance level of  $8\sigma$  in the XMM-Newton data. This flux is consistent with the Chandra flux quoted above. The overlap in the error bars is not large between the two fluxes and this might be indicative of a small residual of point source fluxes in XMM-Newton, but the contamination is small in any case. These independent detections of the X-ray emission with consistent fluxes from Chandra and XMM-Newton is strong evidence for the extended X-ray emission.



**Fig. 3.** Raw X-ray maps from Chandra (left) and XMM-Newton (right) with point sources subtracted. For details of the point source subtraction, the reader is referred to Finoguenov et al. (2009, 2010). The circle is 1 arcmin radius around the group. The source on the bottom-right of the circle is a residual of the point source subtraction. The point source there is the 2nd brightest object in CDFS in the soft-band with a flux of  $4 \times 10^{-14}$  erg s $^{-1}$  cm $^{-2}$  (Xue et al. 2011).

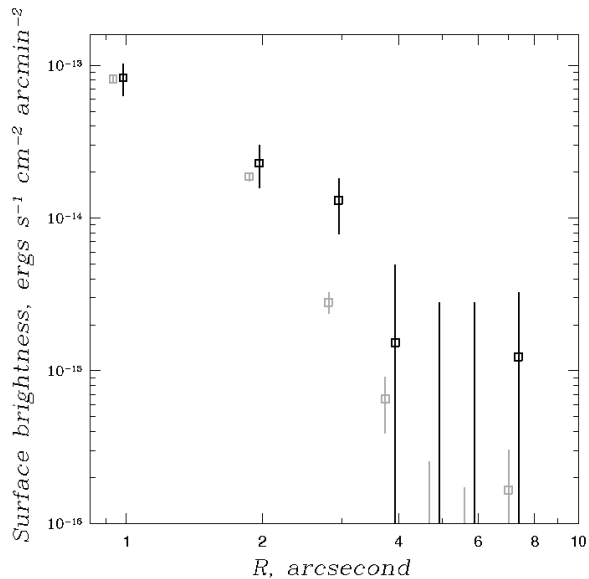


**Fig. 4.** The black squares show the X-ray radial profile of the BGG. For comparison, the gray squares show the profile of a strong AGN separated from the BGG by only 12". At this close proximity, the profiles of these two sources are directly comparable. The points are shifted by 5% in radius for clarity and the AGN profile is normalized to that of BGG at the center.

Based on all the analyses presented here, we conclude that the detected X-ray emission is real and it originates from hot thermal plasma trapped in a deep potential well of the system. We obtain consistent fluxes between Chandra and XMM-Newton, but we base our analysis on the Chandra flux to be conservative in what follows.

Finally, we note that we obtain tentative evidence for a cool core in the group. The compact X-ray emission around the BGG (object-A as defined later) is slightly more extended than the PSF as shown in Fig. 4, although the difference is not large. If confirmed, this group would

be the highest redshift system with a cool core. It may also help explain the galaxy population because a group with a cool core is unlikely to have recently experienced a violent merger event (we will elaborate on this point in Section 5). However, given the large error bars in Fig. 4, the object may well be a faint AGN. BGG is not detected in the 2-8 keV band and the lower limit on the photon index is 1.14 (Xue et al. 2011), which does not rule out either an AGN or cool core origin for the emission.

### 3.3. An over-density of galaxies at $z = 1.6$

Having detected the extended X-ray emission, we now look for the optical counterpart using deep optical-NIR imaging. For this, we have run a red sequence finder as described in Section 2.3. We have detected a  $6.2\sigma$  signal at  $z \sim 1.6$  after calibrating the model red sequence with observed color of galaxies using the MUSIC catalog. No other significant red sequence signal is found at other redshifts. There are three galaxies at  $z_{spec} = 1.03$  within the X-ray contours in Fig. 1, but we argue that they are not the primary counterpart of the X-ray emission in Appendix 1.

In order to define group member candidates, we use  $z_{phot,rafferty}$  and  $z_{phot,tanaka}$ . Given that photo- $z$ 's are sensitive to a change in input photometry and templates, we use both photo- $z$  estimates in order to reduce any systematic uncertainties arising from photo- $z$ 's. We define a member candidate as a galaxy with

$$P_{gr} = \int_{z_{gr}-0.06 \times (1+z_{gr})}^{z_{gr}+0.06 \times (1+z_{gr})} P(z) dz \geq 0.16, \quad (1)$$

where  $z_{gr}$  is the group redshift ( $z_{gr} = 1.61$  as discussed later) and  $P(z)$  is the photometric redshift probability distribution function (PDF) from the fitting procedure. Rafferty et al. (2011)'s photo- $z$ 's have an accuracy of  $\Delta z_{phot,rafferty} / (1 + z_{spec}) = 0.06$  for faint sources. Motivated by this, we integrate the PDF over the interval of  $z_{gr} - 0.06 \times (1 + z_{gr})$  to  $z_{gr} + 0.06 \times (1 + z_{gr})$ . If the integrated probability exceeds 0.16 we define the galaxy

as a group member candidate. In other words, if a galaxy is consistent with being at  $|z_{\text{phot}} - z_{\text{gr}}|/(1 + z_{\text{gr}}) < 0.06$  within  $1\sigma$ , it is a candidate for group membership.

The two photo- $z$ 's agree for most objects, but there are some discrepant cases. We define two categories here:

- *Good candidates* are those with photo- $z$ 's consistent with being at  $z_{\text{gr}}$  (see Eq. 1) both from  $z_{\text{phot,rafferty}}$  and  $z_{\text{phot,tanaka}}$ .
- *Likely candidates* are those that have  $z_{\text{phot,tanaka}}$  consistent with being at  $z_{\text{gr}}$ , while they have lower/higher  $z_{\text{phot,rafferty}}$ . Note that even if both photo- $z$ 's are consistent, an object can fall in this category if its photo- $z$ 's are not very reliable (e.g., bad  $\chi^2$ ).

There is obviously a third category of galaxies with  $z_{\text{phot,rafferty}}$  at  $z_{\text{gr}}$ , but with lower/higher  $z_{\text{phot,tanaka}}$ . There is no such galaxy in the core of the group and we do not include the third category in the following discussions. We refer to the bright ( $H < 24$ ) good/likely candidates as object-X, where X is an upper/lower case letter, respectively, in the order of the  $H$ -band brightness. We do not discuss fainter galaxies in detail because their photo- $z$ 's are uncertain and their field contamination probabilities are high (see Section 3.4). Table 1 summarizes photo- $z$ 's of the candidates.

Now, let us go back to Fig. 1, in which we show the spatial distribution of good and likely candidates. We observe a clear concentration of galaxies at  $z_{\text{phot}} \sim 1.6$  around the extended X-ray emission. Most of them are within the X-ray contours, which roughly corresponds to  $0.5r_{200}$ , where  $r_{200}$  is the radius within which the mean interior density is 200 times the critical density of the universe. The BGG is not at the center of the X-ray emission, but is offset to the West. This might be partly due to a strong concentration of the X-ray point sources in the Eastern part of the system causing low-level contamination. Based on the 3rd nearest-neighbor density using galaxies with  $H < 24$  and  $P_{\text{gr}} \geq 0.16$ , we observe a  $5\sigma$  over-density.

We emphasize that this is not the first detection of an over-density at this redshift in the CDFS. In fact, a large scale structure at this redshift was already found by Kurk et al. (2009), see their Fig. 2. Our group is on the edge of the GOODS field and is located about 5 arcmin (2.5 Mpc) away from the main region of over-density studied by Kurk et al. (2009). In our X-ray map, there are a few low-significance sources around the main Kurk et al. (2009) region, but we defer detailed discussions on the region in Finoguenov et al. (in prep). On the other hand, our group shows the clear extended X-ray emission as discussed above. It is likely the first gravitationally bound, X-ray bright system found in the  $z = 1.6$  structure.

As can be seen in Fig. 1, there are a large number of spectroscopic redshifts from the literature. The BGG is confirmed at  $z = 1.61$ , which gives a strong constraint on the central redshift of the group. Object-C is also confirmed to be a group member, at  $z = 1.625$  (see below). The redshifts indicated in Fig. 1 are secure redshifts only, but there are a large number of less secure spectroscopic

redshifts from the literature. We summarize secure and less secure redshifts around  $z \sim 1.6$  in Fig. 5. We briefly comment on each spectrum below.

**Object-A:** This is the BGG of the group. It exhibits a strong emission line, which is identified as [OII] redshifted by  $z_{\text{spec}} = 1.61$ . The galaxy has  $z_{\text{phot,rafferty}} = 1.60$  and  $z_{\text{phot,tanaka}} = 1.62$ , consistent with the spectroscopic redshift (Table 1). As discussed above, the X-ray emission around object-A might be a cool core. If we translate the observed [OII] luminosity into SFR using the formula from Kennicutt (1998), we obtain a SFR of  $3.6 M_{\odot} \text{ yr}^{-1}$ . We do not apply a correction for slit loss and this SFR is thus a lower limit. As discussed below, we find a SFR of  $< 2 M_{\odot} \text{ yr}^{-1}$  from SED fitting and from the MIPS flux, which is lower than that from [OII]. This suggests that object-A hosts an AGN that contributes to the observed [OII] emission. Tanaka (2011a,b) show that an excess emission line luminosity that cannot be fully accounted for by star formation can be efficiently used to identify AGNs. It is likely that object-A hosts an AGN. It remains unclear whether the slightly extended component is a cool core, but it is possible that the X-ray emission is a combination of point-like AGN and extended cool core.

**Object-B:** This object is given  $z = 1.605$  in the K20 survey (Mignoli et al. 2005) with a low quality flag. There is a possible CIV line, although the feature is not convincing. This galaxy is an X-ray point source and the possible CIV line might be due to the AGN. We note that the photometric redshifts of the galaxy are  $z_{\text{phot,rafferty}} = 1.59$  and  $z_{\text{phot,tanaka}} = 1.64$ , being consistent with the spectroscopic redshift if the feature is real.

**Object-C:** The galaxy shows relatively clear FeII and MgII absorption features. It is given  $z = 1.615$  in the K20 catalog, but we slightly tweak the redshift ( $\Delta z = +0.01$ ) so that we can fit the absorption lines better. However, we do not argue that our redshift is more precise than the original one. Rather, this gives us a level of uncertainty in the redshift. The photo- $z$ 's of this galaxy are  $z_{\text{phot,rafferty}} = 1.56$  and  $z_{\text{phot,tanaka}} = 1.64$ . The K20 catalog assigns a low quality flag to this object, but given the relatively strong absorption features and consistent photo- $z$ , we consider it is a secure redshift.

Overall, we have two secure redshifts from the K20 survey both at  $z \sim 1.61$ . The central redshift of the group is likely the redshift of the BGG,  $z = 1.61$ . An interesting point worth noting here is that three of the nine good/likely candidates are AGNs (objects A, B and g). Table 2 summarizes their absorption corrected X-ray luminosities taken from Xue et al. (2011) together with other physical parameters derived in Section 4. Object-g is a moderately strong AGN with  $L_X \sim 5 \times 10^{43} \text{ erg s}^{-1}$  at 0.5–8 keV<sup>1</sup>. The other two, one of which is BGG, are weak AGNs with  $L_X \sim 4 \times 10^{42} \text{ erg s}^{-1}$ . If we assume that all the six good candidates are group members, we

<sup>1</sup> This object is nominally a good candidate given the consistent  $z_{\text{phot,tanaka}}$  and  $z_{\text{phot,rafferty}}$ . However,  $\chi^2_{\nu}$  of  $z_{\text{phot,tanaka}}$  is bad (see Table 2) and also this object is given  $z_{\text{phot}} = 2.8$  by Xue et al. (2011). We downgrade the object to a likely candidate. We scale its  $L_X$  from  $z = 2.8$  to  $z = 1.6$  and quote it here.



**Table 1.** Photo- $z$ 's and  $P_{gr}$  for good/likely member candidates based on the three different photo- $z$  catalogs. Object-g has  $P_{gr} \geq 0.16$  both from  $z_{tanaka}$  and  $z_{rafferty}$ , but given the poor SED fit shown in Section 4, we classify it only as a likely candidate.

ID	$z_{phot,tanaka}$	$P_{gr,tanaka}$	$z_{phot,rafferty}$	$P_{gr,rafferty}$	$z_{phot,cardamone}$
object-A	$1.62^{+0.08}_{-0.08}$	0.97	$1.60^{+0.03}_{-0.02}$	1.00	$1.61^{+0.02}_{-0.02}$
object-B	$1.64^{+0.06}_{-0.09}$	0.94	$1.59^{+0.03}_{-0.02}$	1.00	$1.62^{+0.03}_{-0.02}$
object-C	$1.64^{+0.06}_{-0.08}$	0.95	$1.56^{+0.03}_{-0.03}$	0.97	—
object-D	$1.59^{+0.26}_{-0.10}$	0.63	$1.58^{+0.34}_{-0.13}$	0.49	$1.67^{+0.05}_{-0.04}$
object-E	$1.56^{+0.07}_{-0.09}$	0.87	$1.41^{+0.04}_{-0.04}$	0.16	—
object-F	$1.64^{+0.12}_{-0.13}$	0.72	$1.67^{+0.05}_{-0.10}$	0.86	—
object-g	$1.57^{+0.23}_{-0.25}$	0.43	$1.59^{+0.07}_{-0.10}$	0.91	$2.94^{+0.11}_{-0.14}$
object-h	$1.61^{+0.11}_{-0.10}$	0.80	$1.18^{+0.06}_{-0.06}$	0.07	—

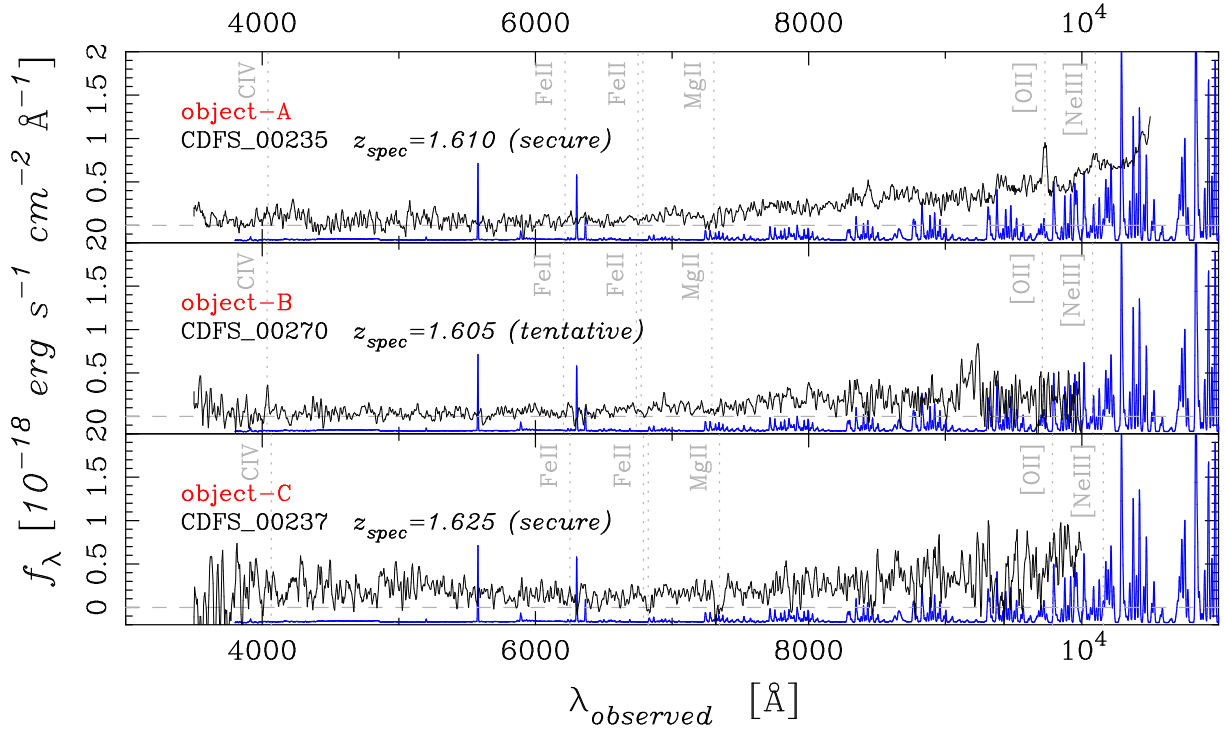


**Fig. 5.** The spectra of three galaxies around the group from the K20 survey (Mignoli et al. 2005). The blue lines are arbitrarily scaled sky spectra (the spectra do not come with associated noise spectra). Prominent spectral features are indicated with labels. The spectra are object-A, B, and C from top to bottom, respectively, and the spectra are smoothed over  $15\text{\AA}$  with a top-hat filter.

obtain an AGN fraction and binomial statistical error of  $0.33_{-0.21}^{+0.28}$ . If we include likely candidates, this fraction becomes  $0.38_{-0.20}^{+0.23}$ . Although the uncertainty is large, such a high fraction of X-ray AGNs has not been observed in any other cluster. Martini et al. (2007) reported that a fraction of AGNs with  $L_X > 10^{42}$  erg s $^{-1}$  hosted by  $M_R < -20$  mag galaxies, which very roughly matches with our selection of group members in terms of stellar mass, is about 1% in local clusters. Previous studies have shown that the AGN fraction in clusters seems to increase with increasing redshift (Eastman et al. 2007; Martini et al. 2009). An increasing AGN fraction is also observed in a spectroscopic study (Tanaka et al. 2011). Recently, Fassbender et al. (2012) reported on a detection of AGNs in high- $z$  clusters. This group may extend this increasing AGN fraction to higher redshifts. However, a larger sample of groups at this redshift is obviously needed to establish it.

Finally, we note that there is a bright red galaxy whose photo- $z$ 's are consistent with  $z = 1.6$  ( $z_{phot,tanaka} = 1.63$ ,  $z_{phot,rafferty} = 1.45$ , and  $z_{phot,cardamome} = 1.57$ ), but its secure emission-line redshift from the K20 spectrum is  $z = 1.149$ . The object is located at R.A. =  $03^{\text{h}}32^{\text{m}}13^{\text{s}}.01$ , Dec. =  $-27^{\circ}46'37''.9$ , just outside of the group X-ray emission in Fig. 1. We cannot fit the SED of this object at  $z = 1.149$  with any reasonable  $\chi^2$  and there are also large residuals after subtracting the best-fit model galaxy for the morphological analysis described in Section 5. It is possible that there are two overlapping galaxies with the brighter galaxy at  $z \sim 1.6$  dominating the overall flux, and the fainter one at  $z = 1.15$  responsible for the emission line in the spectrum. Deep near-IR spectroscopy of the object will be useful to measure its continuum redshift. To be conservative, we do not include this object in the analysis.

### 3.4. Color-magnitude diagrams

A ubiquitous feature of rich galaxy groups and clusters in the low redshift Universe, in addition to over-density of galaxies, is the tight red sequence. Red, passively evolving galaxies in groups and clusters form a sequence of galaxies on the color-magnitude diagram with a shallow tilt due to the mass-metallicity relation (Kodama & Arimoto 1997). The group fortunately falls within the footprint of CANDELS, providing publicly available, high quality, deep optical and near-IR HST images. Based on the CANDELS data, we present  $I - J$  vs  $J$  and  $I - H$  vs  $H$  diagrams in Fig. 6.

The photo- $z$  selected galaxies with  $P_{gr} \geq 0.16$  form a surprisingly prominent red sequence. There are 2 secure members and 6 membership candidates with  $H < 24$  in the group. Strikingly, a significant fraction have red colors on both diagrams. The brightest galaxy (A) is slightly redder than the other galaxies and is consistent with being formed at  $z_f = 5$ . The remaining galaxies are on the model red sequence formed at  $z_f = 3$  with two exceptions. Object-g is located near the  $z_f = 2$  sequence, but this object is a powerful X-ray point-source and the photometry may be affected by the central AGN. Object-D is clearly bluer, and is forming stars as shown in the next section. We find that – except for these two objects – all massive

galaxies are classified using a color-color diagram (e.g., Williams et al. 2009; Balogh et al. 2009) as passive, not as dusty star forming galaxies. There are a few faint blue galaxies with  $H > 24$  and  $P_{gr} \geq 0.16$ , but the bright members are almost exclusively red.

We argue here that the dominance of bright red galaxies is not due to biases in the photo- $z$ 's. Photo- $z$ 's tend to be more accurate for quiescent galaxies than for star forming ones due to the prominent 4000Å break of quiescent galaxies. This bias may result in an enhanced red fraction, but as shown in Fig. 6, a significant fraction of bright blue galaxies have secure spec- $z$ 's and none of them is at the group redshift. This is strong evidence for the bright group members being predominantly red. We further note that our photo- $z$ 's are reasonably good even for blue galaxies. We find that, for  $z_{phot,rafferty}$ , an outlier rate<sup>2</sup> of red galaxies with  $I - H > 1.5$  (which roughly selects red sequence galaxies) at  $1 < z_{spec} < 2$  is  $8 \pm 3\%$ . The outlier rate for bluer galaxies is slightly larger;  $12 \pm 3\%$ . The outlier rates are similar for  $z_{phot,tanaka}$ ;  $7 \pm 3\%$  and  $14 \pm 3\%$  for red and blue galaxies, respectively. In both photo- $z$ 's, the dispersion is 20% larger for blue galaxies than for red galaxies. Photo- $z$ 's are indeed better for red galaxies, but even for blue galaxies, the outlier rate is only  $\sim 13\%$ . There are 8 galaxies with  $H < 24$  and  $I - H < 1.5$  that do not have spec- $z$ 's. Even if we miss 1 blue galaxy among them, it is still fair to say that the bright group galaxies are mostly red.

The dominance of bright red galaxies is surprising in a low mass group at such a high redshift. The red sequence extends to  $H \sim 23.5$ , which corresponds to  $\sim m_H^* + 2$ . There is no photo- $z$  selected red sequence galaxy at fainter magnitude, suggesting a truncation of the red sequence. This truncation magnitude ( $m^* + 2$ ) is similar to that observed in groups at  $z = 1.2$  (Tanaka et al. 2007)<sup>3</sup>. However, we should be reminded that photo- $z$ 's become less accurate at fainter magnitudes. The apparent truncation might be partly due to increased errors in the photo- $z$ 's.

We further check if the observed red sequence is real using statistical subtraction of fore-/background galaxies without relying on photo- $z$ 's. Using the recipe described by Tanaka et al. (2005), we compute a probability that a given galaxy is in the fore-/background (i.e. contamination). We use the entire CDFS CANDELS field as a control sample for the field subtraction. Fig. 7 shows the contamination probability of each galaxy. We do not take a Monte-Carlo approach for the statistical subtraction as done by Tanaka et al. (2005); instead we explicitly show the contamination probability. It is clear that the bright galaxies on the red sequence are unlikely to be contamination. There is only a small statistical probability that any of the photo- $z$  selected good or likely members from Fig. 6 are fore-/background galaxies, and Fig. 7 shows

<sup>2</sup> Outliers here are defined as those with  $|z_{phot} - z_{spec}| / (1 + z_{spec}) > 0.15$  following the standard definition.

<sup>3</sup> Tanaka et al. (2007) used the  $K_s$ -band to measure the truncation magnitude, while we use the  $H$ -band here. However, we focus only on passive galaxies, and the truncation magnitude does not depend on a pass-band when expressed with respect to  $m^*$ .

**Table 2.** Physical properties of galaxies derived from the SED fits along with absorption-corrected X-ray luminosities at rest-frame 0.5–8.0 keV from Xue et al. (2011) and SFRs from MIPS assuming the MIPS to total IR luminosity conversion from Reddy et al. (2006) and to SFRs using Kennicutt (1998). MIPS fluxes are taken from the MUSIC catalog (Santini et al. 2009). We fit the SEDs of object-A and C with redshifts fixed to their spectroscopic redshifts. Object-g is contaminated by AGN and so we fail to reliably measure its stellar mass and SFR from the SED fits or from MIPS. Also, this object was assigned  $z_{phot} = 2.8$  in Xue et al. (2011). We rescale the X-ray luminosity to  $z = 1.6$ . The quoted uncertainties are statistical uncertainties only.

ID	$\chi_\nu$	$z_{phot,tanaka}$	$M_{stellar} [10^{10}M_\odot]$	SFR [ $M_\odot \text{ yr}^{-1}$ ]	$L_X [10^{42} \text{ erg s}^{-1}]$	SFR <sub>MIPS</sub> [ $M_\odot \text{ yr}^{-1}$ ]
object-A	1.6	$z_{spec} = 1.61$	$31.6^{+0.1}_{-13.9}$	$0.79^{+0.03}_{+0.01}$	4.3	< 2.0
object-B	0.3	$1.64^{+0.06}_{-0.09}$	$7.9^{+1.1}_{-0.1}$	$0.06^{+0.16}_{-0.01}$	4.7	$1.5 \pm 0.6$
object-C	0.6	$z_{spec} = 1.62$	$4.5^{+0.1}_{-0.1}$	$0.03^{+0.01}_{-0.01}$	—	< 1.4
object-D	0.7	$1.59^{+0.26}_{-0.10}$	$1.4^{+1.2}_{-0.4}$	$22.91^{+13.41}_{-4.71}$	—	$25 \pm 1$
object-E	0.2	$1.56^{+0.07}_{-0.09}$	$1.8^{+1.1}_{-0.6}$	$0.05^{+0.08}_{-0.04}$	—	$0.6 \pm 0.6$
object-F	0.4	$1.64^{+0.12}_{-0.13}$	$1.3^{+0.6}_{-0.4}$	$0.06^{+0.04}_{-0.03}$	—	< 1.9
object-g	2.5	$1.57^{+0.23}_{-0.25}$	—	—	49	—
object-h	0.3	$1.61^{+0.11}_{-0.10}$	$0.6^{+0.4}_{-0.2}$	$0.08^{+0.32}_{-0.06}$	—	< 1.3

that the red sequence is clearly real. There are many faint, blue galaxies around the group, but most of them are likely to be fore-/background galaxies as indicated by their large contamination probabilities. There seems to be a few sheets of structure in the foreground of the group and bright blue galaxies have somewhat small contamination probabilities. But, most of them are spectroscopically confirmed foreground galaxies as shown in Fig. 6.

To sum up, there is plenty of evidence to support the convincing detection of an X-ray group at  $z = 1.6$  in the CDFS. First, the extended X-ray emission is detected, which strongly suggests that this is a physically bound system. Second, a clear over-density of galaxies is observed around the X-ray emission at  $z_{phot} \sim 1.6$ . The BGG is spectroscopically confirmed at  $z = 1.61$ , which is likely the central redshift of the group. Third, the member candidates form a tight red sequence. All these results lead us to conclude that this is a galaxy group located at  $z = 1.61$ .

### 3.5. X-ray Properties of the Group

Using the group redshift of  $z = 1.61$ , we summarize physical properties of the group measured from X-rays in Table 3. From the X-ray luminosity, we estimate the mass of the group using the calibration against weak-lensing mass from Leauthaud et al. (2010):

$$\frac{M_{200}E(z)}{M_0} = A \left( \frac{L_X E(z)^{-1}}{L_{X,0}} \right)^\alpha, \quad (2)$$

where  $E(z) = \sqrt{(1+z)^3 \Omega_M + \Omega_\Lambda}$ ,  $M_0 = 10^{13.7} M_\odot$ ,  $L_{X,0} = 10^{42.7} \text{ erg s}^{-1}$ ,  $\log(A) = 0.03 \pm 0.06$ ,  $\alpha = 0.64 \pm 0.03$ . This group turns out to be a low-mass system with  $M_{200} = (3.2 \pm 0.8) \times 10^{13} M_\odot$ . The uncertainty here include X-ray flux uncertainty and the scatter in the  $M_{200} - L_X$  relation. There is a possible Eddington bias that this group is over-bright for its mass, but its effect is estimated to be  $\lesssim 10\%$  (Leauthaud et al. 2010). The  $M_{200} - L_X$  relation used here is measured at  $z < 1$  and we have extrapolated it to  $z = 1.6$ . This will introduce a systematic error, amount of which is not straightforward to estimate because no calibration is available at  $z > 1$  due to the lack of statistical sample of groups and clusters there. At any

rate, it is likely the lowest mass system confirmed so far at  $z > 1.5$  (c.f.  $6 \times 10^{13} M_\odot$ , the mass of another  $z = 1.6$  group in SXDF measured in the same way, Tanaka et al. 2010). Such a high- $z$  low-mass group is an interesting object to study the origin of the environmental dependence of galaxy properties and may be an early progenitor which will grow into a present-day cluster. Motivated by this, we perform detailed analyses of the properties of the group members in the following sections.

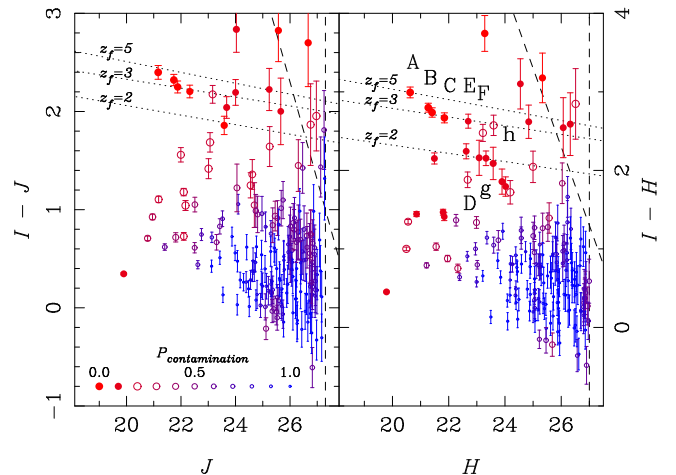


**Fig. 7.** The same color-magnitude diagram as in Fig. 6, but here we do not use photometric redshifts. We instead perform statistical subtraction of fore-/background galaxies. Galaxies with smaller, bluer symbols are more likely to be contamination.

## 4. Stellar Populations of the Group Members

### 4.1. Spectral energy distribution fitting

As shown in Section 3, the group consists of 8 relatively bright galaxies, most of which have red colors. In this section, we attempt to put tighter constraints on the stellar populations of the galaxies by using the multi-wavelength data from MUSIC (Santini et al. 2009).

We fit the observed broad-band photometry with a

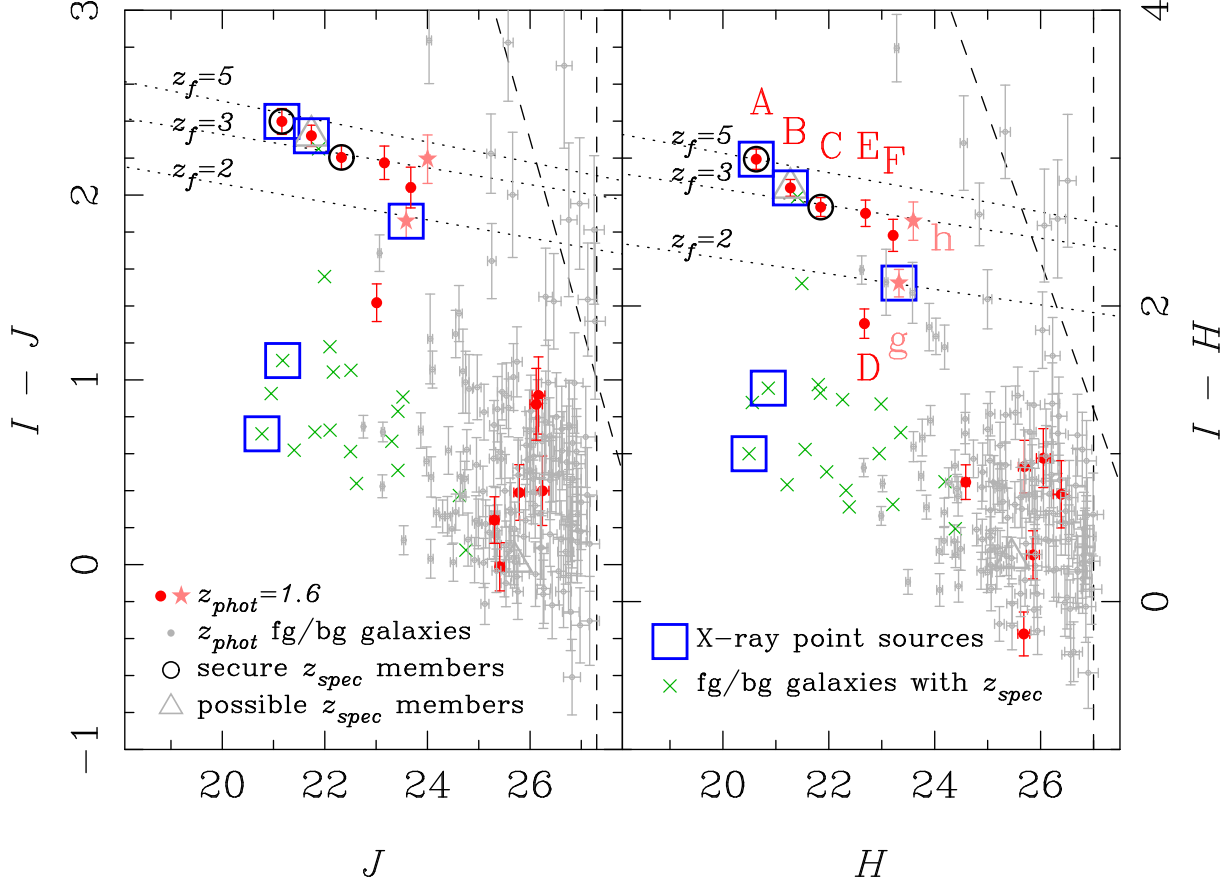


**Fig. 6.** Color-magnitude diagrams based on the CANDELS data. The left and right panels respectively show  $I - J$  vs.  $J$  and  $I - H$  vs.  $H$ . All the galaxies within  $r_{200}$  of the group center are plotted here. The large points are galaxies with  $P_{gr} \geq 0.16$ . Among them, the red/pink symbols with  $H < 24$  are the good/likely candidates selected from photo- $z$  and are labeled as object-A to h in the order of the  $H$ -band magnitude. The gray points are fore-/background galaxies based on photo- $z$ . The dark circles and light triangles indicate secure and possible spectroscopic members, respectively. The crosses indicate fore-/background galaxies with secure spec- $z$ 's. The blue squares show X-ray sources. The vertical and slanted dashed lines are  $5\sigma$  limits. The dotted lines show model red sequence of galaxies formed at  $z_f = 2, 3$ , and 5.

**Table 3.** Physical properties of the group measured from X-ray. The 3rd and 4th columns show the X-ray flux in the observed 0.5 – 2.0 keV band and X-ray luminosity at rest-frame 0.1–2.4 keV both within  $r_{500}$  (this is a radius, within which the mean interior density is 500 times the critical density of the universe). For details of the flux estimate, refer to Finoguenov et al. (2007). The 5th column is  $r_{200}$  and the last column shows  $M_{200}$ , which is mass contained within  $r_{200}$  calibrated against weak-lensing mass at  $z < 1$  (Leauthaud et al. 2010). The uncertainties quoted are statistical only and our  $M_{200}$  estimate is subject to systematic uncertainties (see text for details).

R.A.	Dec.	$f_X$ (0.5 – 2 keV)	$L_X$ (0.1 – 2.4 keV)	$r_{200}$	$M_{200}$
$03^h 32^m 11^s.7$	$-27^\circ 46' 34''$	$(3.1 \pm 1.0) \times 10^{-16} \text{ erg s}^{-1} \text{ cm}^{-2}$	$(1.8 \pm 0.6) \times 10^{43} \text{ erg s}^{-1}$	44" or 370 kpc	$(3.2 \pm 0.8) \times 10^{13} M_\odot$

suite of model templates generated with an updated version of the Bruzual & Charlot (2003) code, which incorporates an improved treatment of the thermally pulsating AGB stars. Given that most of the group galaxies exhibit red colors, it is reasonable to assume exponentially declining star formation histories (c.f., Maraston et al. 2010). We assume the Chabrier IMF (Chabrier 2003) and solar metallicity for all the models. Model parameters such as age and metallicity are degenerate and we prefer to use solar metallicity models only because super-solar or sub-solar metallicity models introduce larger degeneracies and they do not reproduce the

mass-metallicity relation (Tanaka 2011a). We use the attenuation law from Calzetti et al. (2000). We fit the observed photometry ( $u_{VIMOS}$ ,  $u_{38}$ ,  $u_{50}$ ,  $B$ ,  $V$ ,  $R$ ,  $I$ ,  $z$ ,  $J$ ,  $H$ ,  $K_s$ ,  $3.5\mu m$ ,  $4.6\mu m$ ,  $5.7\mu m$ ,  $8.0\mu m$ ) with the model templates in the linear flux scale using the standard  $\chi^2$ -minimizing technique.

Model templates do not always perfectly match with the observed SEDs of galaxies and we apply a crude correction to the templates to reduce the SED mismatches. We use galaxies with spectroscopic redshifts drawn from the literature and fit them with redshifts fixed to their spectroscopic redshifts using the MUSIC photometry. Because

the spectroscopic galaxies span a wide range in redshift, the observed photometry covers a wide range of rest-frame wavelengths. By comparing observed fluxes with the best-fitting model fluxes, we measure systematic flux stretches in the model templates as a function of rest-frame wavelength. We also measure a flux dispersion, which can be used as an uncertainty in the models at a given wavelength. We apply this template error function to all the templates used in the SED fitting. For details, the reader is referred to Appendix 2. We note that the template error function increases errors on all the parameters derived from the SED fitting, but we deem that the increased errors are more realistic estimates. Note as well that the template error function does not completely remove the systematics. There are remaining systematics arising from, e.g., the assumption of the star formation histories of galaxies, but they are more difficult to evaluate and are not corrected for in this paper.

For object-g, which is a strong X-ray source, we use a set of composite templates of AGNs and galaxies. We use AGN templates from Polletta et al. (2007) and apply extinction of  $\tau_V = -0.2, 0, +0.2$  and  $+0.4$ . The negative extinction makes sense because the empirical templates already include extinction. We restrict galaxy templates to relatively young ages of  $< 3$  Gyr with  $\tau = 1$  Gyr. We then normalize the spectra at  $5500\text{\AA}$  and merge an AGN template and a galaxy template with ratios of 1:2, 1:1, 2:1 and 4:1. We fit object-g using these AGN-galaxy composite templates.

The results of the fitting for the six good candidates are shown in Fig. 8 and the two likely candidates in Fig. 9. The derived physical parameters of the galaxies are summarized in Table 2. For object A and C, we perform the SED fitting with redshifts fixed to their spectroscopic redshifts. The fits are generally good and the objects are consistent with being located at  $z \sim 1.6$ . Object-D is very close to BGG and its photometry in the IRAC bands is severely contaminated by the BGG. Therefore, we remove the IRAC photometry from the SED fit. All the galaxies except for object-g show a prominent  $4000\text{\AA}$  break in between the  $z$  and  $J$ -bands. This strongly suggests that the galaxies have old stellar populations, as expected from the tight red sequence.

In Section 3, we defined *likely* candidates as those with discrepant photo- $z$ 's between ours and Rafferty et al. (2011) or those with a poor SED fit. Let us briefly mention the two likely candidates in Fig. 9. The fit for object-g is not very good, but it is a strong X-ray source and the bad fit might be due to variability (e.g.,  $U_{50}$  is much brighter than the other  $U$ -band photometry). Although we have consistent photo- $z$ 's both from  $z_{phot,tanaka}$  and  $z_{phot,rafferty}$ , the fit is not very good ( $\chi^2_\nu = 2.5$  including the template error). Due to this bad fit, we define this galaxy as a likely candidate. For object-h, we have inconsistent photo- $z$ 's:  $z_{phot,tanaka} = 1.61$  and  $z_{phot,rafferty} = 1.18$ . However, our fit is very good as shown in Fig. 9. Also, the galaxy is on the red sequence (Fig. 6) and is spatially located close to the center of the group. For these reasons, we include it in our analysis as a

likely candidate. We note that the primary conclusions of this paper do not significantly change if we exclude these likely candidates.

#### 4.2. Physical properties

Now, let us turn our attention to the physical properties of the galaxies derived from the SED fits. We find that the BGG has a stellar mass of about  $3_{-1}^{+0} \times 10^{11} M_\odot$ , which is  $\gtrsim 3$  times more massive than the 2nd most massive galaxy (object-B). If we integrate the stellar mass of the good/likely group members, we obtain  $\sim 5_{-2}^{+0} \times 10^{11} M_\odot$ . Object-g is excluded here because our stellar mass estimate is not very reliable due to the AGN contamination, but it probably does not significantly contribute to the overall stellar mass budget given its faint  $H$ -band magnitude (it is about 3 magnitudes fainter than the BGG). Also, we do not include faint galaxies with  $H > 24$  in the statistics here, and thus the number quoted here is a lower limit. However, the total stellar mass is dominated by the few brightest galaxies and it is unlikely to change significantly if we included those low-mass galaxies. The stellar mass to total mass ratio within  $r_{200}$  is then  $\sim 2\%$ . This fraction is nearly a factor of 2 smaller than that observed at  $z < 1$  by Giodini et al. (2009), but it is consistent with more recent estimates by Leauthaud et al. (2012) and Connelly et al. (2012 submitted).

The most striking result here is that the group galaxies have very low SFRs for  $z = 1.6$  galaxies ( $< 0.1 M_\odot \text{yr}^{-1}$ ). We recall that SFRs quoted in Table 2 are subject to systematic uncertainty due to the assumption of the exponentially declining SFRs. Also, SFRs from SED fits may not be very precise at low SFRs (Pacifi et al. 2012). However, most of the objects are actually not detected in the very deep MIPS data at a significant level as shown in Table 2, which gives independent evidence for very low SFRs of the group galaxies. Only object-D is detected in MIPS at a significant level and its SFRs from the SED fitting and MIPS are consistent ( $\text{SFR} \sim 20 M_\odot \text{yr}^{-1}$ ). The BGG is likely forming stars at a low rate of  $\sim 1 M_\odot \text{yr}^{-1}$ , which is consistent with the upper limit from the MIPS flux. The only object with active star formation is object-D and it is actually bluer than the red sequence in Fig. 6.

To quantify how quiescent the group galaxies are, we show a SFR vs stellar mass diagram in Fig. 10. Star forming galaxies form a sequence on this diagram (Elbaz et al. 2007; Noeske et al. 2007) and we show a sequence for star forming galaxies in the field at  $1.5 < z < 2.5$  from Wuyts et al. (2011). Our group is at the lower bound of the redshift range, but a sequence at  $0.5 < z < 1.5$  shifts downwards only by  $\sim 0.3$  dex (Wuyts et al. 2011) and our conclusion here remains unchanged. As shown in Fig. 10, most of the  $z = 1.6$  galaxies are far below the sequence and they have 2–3 orders of magnitude lower SFRs. Only object-D is consistent with the star forming sequence. This clearly shows that the  $z = 1.6$  group galaxies have suppressed star formation. In this case, there is no evidence that the group environment has led to enhanced star formation.

We note that Quadri et al. (2012) quoted a quies-

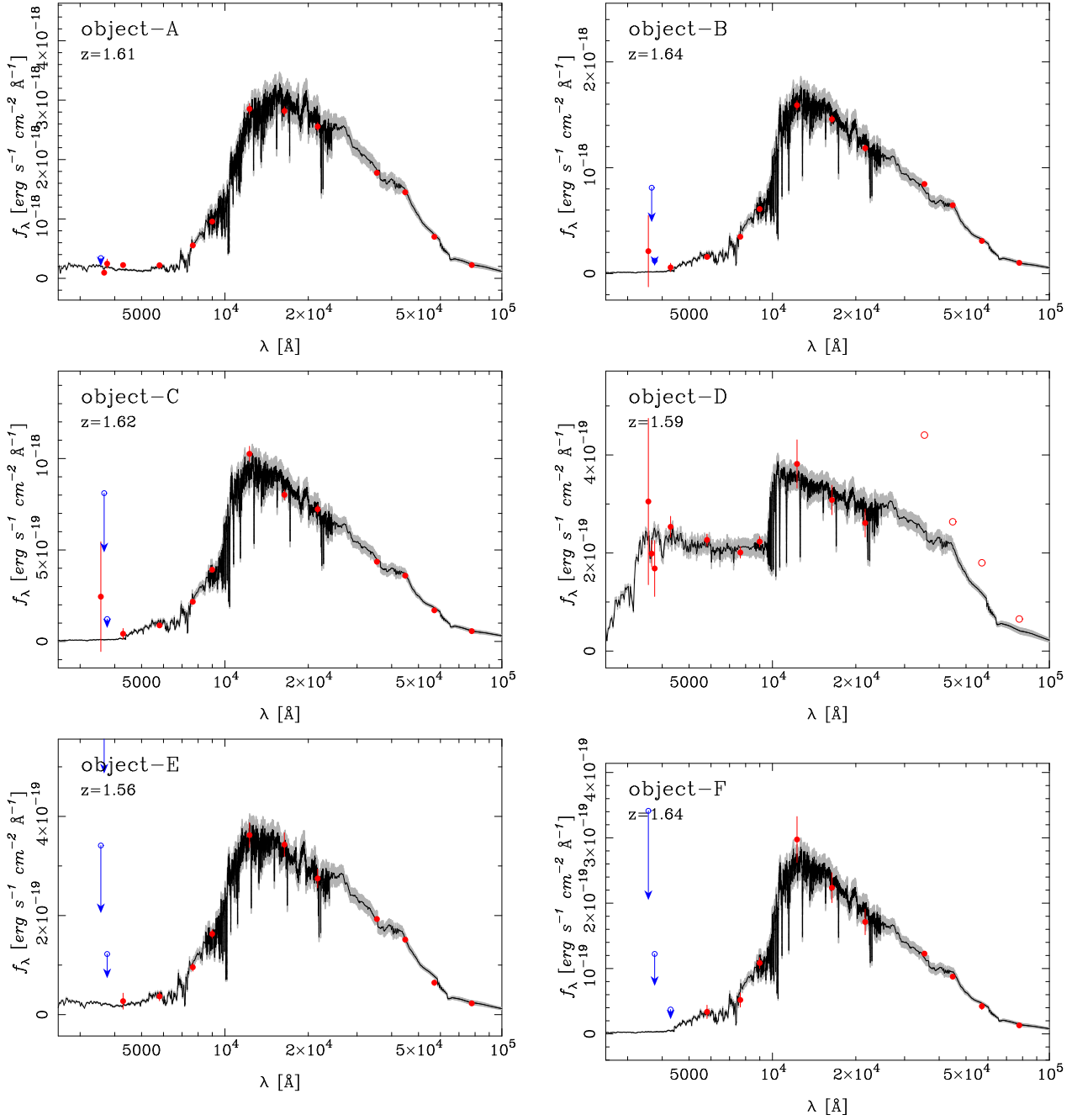


**Fig. 8.** The best-fit model spectra over-plotted with the observed photometry for object A to F. The shaded areas around the best-fit spectra show the template uncertainties derived in the Appendix 2. The best-fit redshift is labeled in each plot. For object-A and C, the fits are performed at  $z_{spec}$ . The points with arrows are upper limits. Object-D is close to the BGG and its IRAC photometry is over-estimated due to the blending. We do not use the IRAC photometry for the SED fitting for this object.

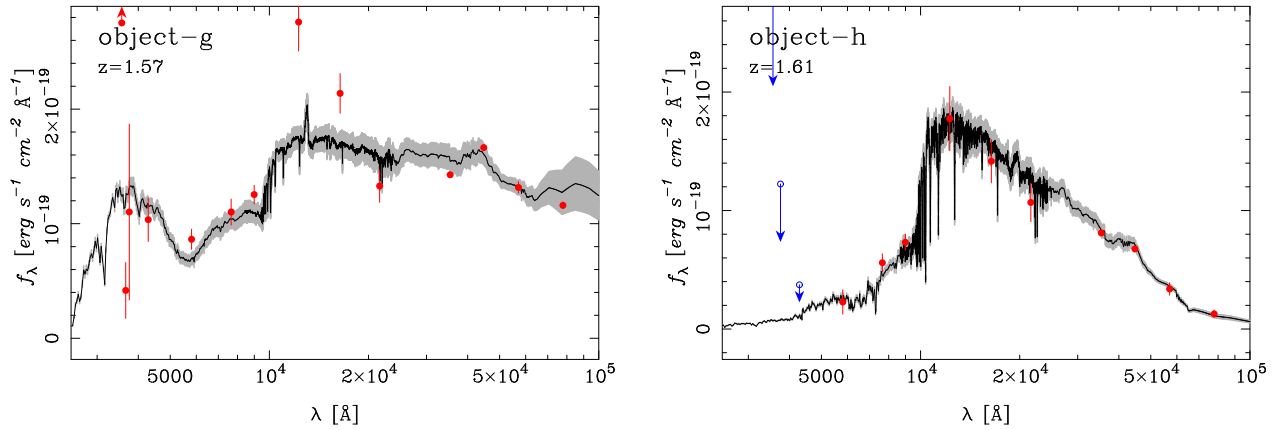


Fig. 9. As in Fig. 8, but for object g and h.

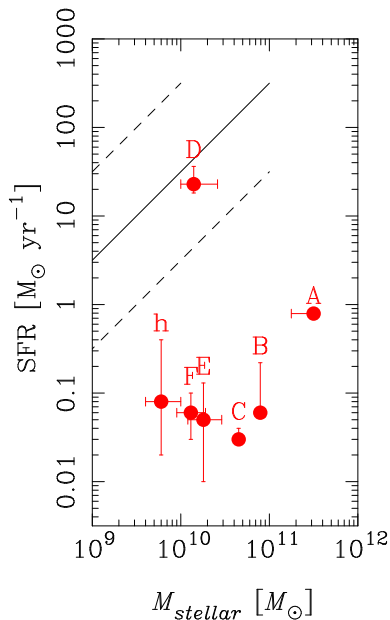


Fig. 10. SFR plotted against stellar mass. The solid line shows a sequence of star forming galaxies at  $1.5 < z < 2.5$  (Wuyts et al. 2011). The dashed lines show an approximate width of the sequence ( $\pm 1$  dex). The large symbols are the  $z = 1.6$  galaxies. Object-g is not plotted here because we cannot measure its SFR.

cent fraction of  $\sim 40\%$  in the densest environment at  $1.5 < z < 2.0$  for galaxies with  $> 10^{10.2} M_{\odot}$ . If we use object-A to F, which have  $\gtrsim 10^{10.2} M_{\odot}$ , the quiescent fraction in the group is  $83_{-29}^{+14}\%$ . Also, Popesso et al. (2012) studied a total SFR within a cluster normalized by the cluster mass and showed that the normalized SFR increases towards higher redshifts. They studied the system found by Kurk et al. (2009) at  $z = 1.6$  in CDFS and measured a normalized total SFR of  $\sim 500 M_{\odot} \text{ yr}^{-1} / 10^{14} M_{\odot}$ . If we use object-A to h, we obtain  $\sim 80 M_{\odot} \text{ yr}^{-1} / 10^{14} M_{\odot}$  for our group, which is a factor of 6 lower than the Kurk et al. (2009) system. These results further illustrate that the group is a fairly quiescent place for  $z = 1.6$ .

To summarize, we have shown that the group is dominated by red galaxies with very low SFRs. Even galaxies with  $\sim 10^{10} M_{\odot}$  are not actively forming stars. These galaxies clearly fall below the sequence of star forming galaxies (Fig. 10). This is a surprising result that the environmental dependence of galaxy star formation is already in place at  $z = 1.6$  in this group. It might suggest that at least some groups are dominated by red, quiescent galaxies from early times. But, let us defer further discussions on this point to Section 6 and focus on another important aspect of galaxies – morphology – in the following section.

## 5. Morphologies of the Group Members

### 5.1. Surface brightness fitting

For the morphological analysis, we use GALFIT (Peng et al. 2002; Peng et al. 2010) to measure structural parameters of the group galaxies. GALFIT performs two-dimensional surface brightness fitting of a galaxy using an input image, a bad pixel map, a PSF image, and noise image. We use the WFC3 F160W image from CANDELS, which probes the rest frame  $r$ -band at  $z = 1.6$ , as an input image of the group. We use a nearby unsaturated star for the PSF image. The noise image is generated from the weight map (Koekemoer et al. 2011). We fit the galaxies with a single Sérsic profile.

Due to the fact that a galaxy group is crowded with galaxies by definition, one must decide how to determine the boundary of the galaxy of interest and how to exclude the neighboring objects' light from a fit. We attempt to solve these problems by defining elliptical regions around the galaxy of interest and neighboring objects to specify their boundaries. The elliptical regions are determined using Source Extractor (Bertin & Arnouts 1996). After some experiments, we find that 6 and 2.5 times of half-light radius are respectively optimum for the galaxy and neighboring objects. A larger radius for the object of interest is necessary as it must contain not only light from the outskirts of the galaxy, but also the sky background. All the initial values for the fitting parameters (position of galaxy

center, integrated magnitude, half-light radius, axis ratio, position angle, Sérsic parameter) are set to those derived by Source Extractor except for the last parameter. The initial Sérsic index is set to 2, which is a boundary of early and late-type galaxies so that we do not bias our fits.

Figs. 11 and 12 show the input image, best-fit model image, residuals, and mask image for the good and likely candidates, respectively. The fits are generally good and the residuals are relatively small for most objects. This verifies that the assumption of a single Sérsic profile is reasonable. We fail to fit object-D due to its irregular morphology and to its close proximity to the BGG.

Here we focus on two of the most important structural parameters; Sérsic index ( $n$ ) and half-light radius. We quote half-light radius as  $r_{50} \equiv \sqrt{ab}$ , where  $a$  and  $b$  are half-light radius measured along the semi-major and semi-minor axes, respectively. We estimate an error on each of the Sérsic index and half-light radius by Monte-Carlo simulations. First, we generate the same background level as in the real  $H$ -band data assuming Gaussian noise and place a model galaxy with a given brightness, effective radius and Sérsic index. We then run GALFIT and measure the structural parameters. We allow the brightness, effective radius, and Sérsic index to vary and repeat the analysis above. A difference between the input and output parameters is fairly small (a few percent) for bright objects with  $H < 22$  mag. For fainter objects, the systematic offset and dispersion increases to 5% and 10% respectively for objects with  $H = 23$  mag. This is roughly the average brightness of the objects that we study in this section. For objects with  $H = 24$ , we measure a 10% systematics and a 20% scatter. We note that all of the objects studied here are brighter than  $H = 24$ .

We then perform another set of simulation. We generate background noise of the same level as in the real data assuming Gaussian noise and place the group members at the same relative location with the same Sérsic indices and half-light radii as the values measured in the CANDELS image for each galaxy. We exclude object-D because we fail to fit this object and therefore cannot use the fitted parameters for the simulation. We then run GALFIT on a simulated image and store the output parameters. We repeat this procedure on 2000 simulated images and adopt the 68% interval of the output parameters as errors. In the figures, we show this error or the error estimated in the first simulation, whichever is larger. In most cases, the latter error is larger. For systematic offsets, we find that the input parameters and the median of the output parameters agree within 10% for all the galaxies. This is consistent with the systematic offsets estimated in the first simulation and this 10% is a reasonable estimate of the systematics.

As shown in Fig. 1, there are a few X-ray point sources among the group member candidates. This X-ray emission is likely due to nuclear activity. To make sure, the presence of AGN does not impact our analysis, we repeat the GALFIT analysis with the central 3 pixels in radius masked out. The derived structural parameters are summarized in Table 4. We also show axial ratios ( $b/a$ ) for

reference. Note that the structural parameters derived with the central masking do not differ significantly from those derived without it.

## 5.2. Structural properties

Let us now compare the structural parameters of the group galaxies with those measured at  $z = 0$  to quantify the morphological evolution. For this comparison, we use data from the Sloan Digital Sky Survey (York et al. 2000). We use galaxies in the Main sample (Strauss et al. 2002) located at  $0.05 < z < 0.07$ . The F160W filter of WFC3 probes rest-frame  $\sim 6000\text{\AA}$  at  $z = 1.6$ , which is very close to the effective wavelength of the  $r$ -band filter in SDSS (Doi et al. 2010). Therefore, the morphological  $k$ -correction is negligible. The PSF of the stacked F160W image is 0.2 arcsec, which corresponds to 1.7 kpc at  $z = 1.6$ . The average seeing in SDSS is 1.5 arcsec, which is also 1.7 kpc at the median redshift of our SDSS sample. The surface brightness limit is much deeper for SDSS than for the  $z = 1.6$  galaxies. But, we have performed a Monte-Carlo simulation to quantify uncertainties on our structural parameter estimates at  $z = 1.6$  as described above and the shallow limit at  $z = 1.6$  is folded into the uncertainty. For the Sérsic index and half-light radius of  $z = 0$  galaxies, we use the New-York University Value Added Catalog (Blanton et al. 2005). The stellar mass for the SDSS sample is taken from Tanaka (2011a) who fitted the SDSS spectra with Bruzual & Charlot (2003) model templates assuming the Chabrier IMF. Note that a correction for the fiber loss is applied in a crude way by assuming that the light within a fiber is representative of the light from the entire galaxy.

Fig 13 presents the Sérsic index,  $n$ , and half-light radius plotted against stellar mass. As can be seen in the left panel, most of the  $z = 0$  galaxies have Sérsic index between 1 and 2. This is the typical range for late-type galaxies. The index shows a tail towards a larger index at high mass, which shows that most massive galaxies tend to be early-type galaxies. We separate early and late-type galaxies at the Sérsic index of  $n = 2$  as shown by the horizontal dashed line in the left panel. If we turn our attention to the  $z = 1.6$  galaxies shown as the large circles in the left panel, we find that most of them have  $n > 2$ . In other words, most of the galaxies in the  $z = 1.6$  group are early-type galaxies. We know that groups and clusters at  $z = 0$  are dominated by early-type galaxies (Dressler 1980; Postman & Geller 1984), but it is surprising that a group at such a high redshift is also dominated by early-type galaxies. We have shown in the previous section that these galaxies are mostly quiescent galaxies. Therefore, the group appears fairly similar to groups and clusters in the local universe.

In addition to the Sérsic index, another interesting structural parameter of galaxies is their physical size. The size evolution is particularly interesting given the recent observations that distant quiescent galaxies are compact compared to  $z = 0$  counterparts (e.g., Daddi et al. 2005; Trujillo et al. 2006; Toft et al. 2007). It would therefore be interesting to study whether the size evolution



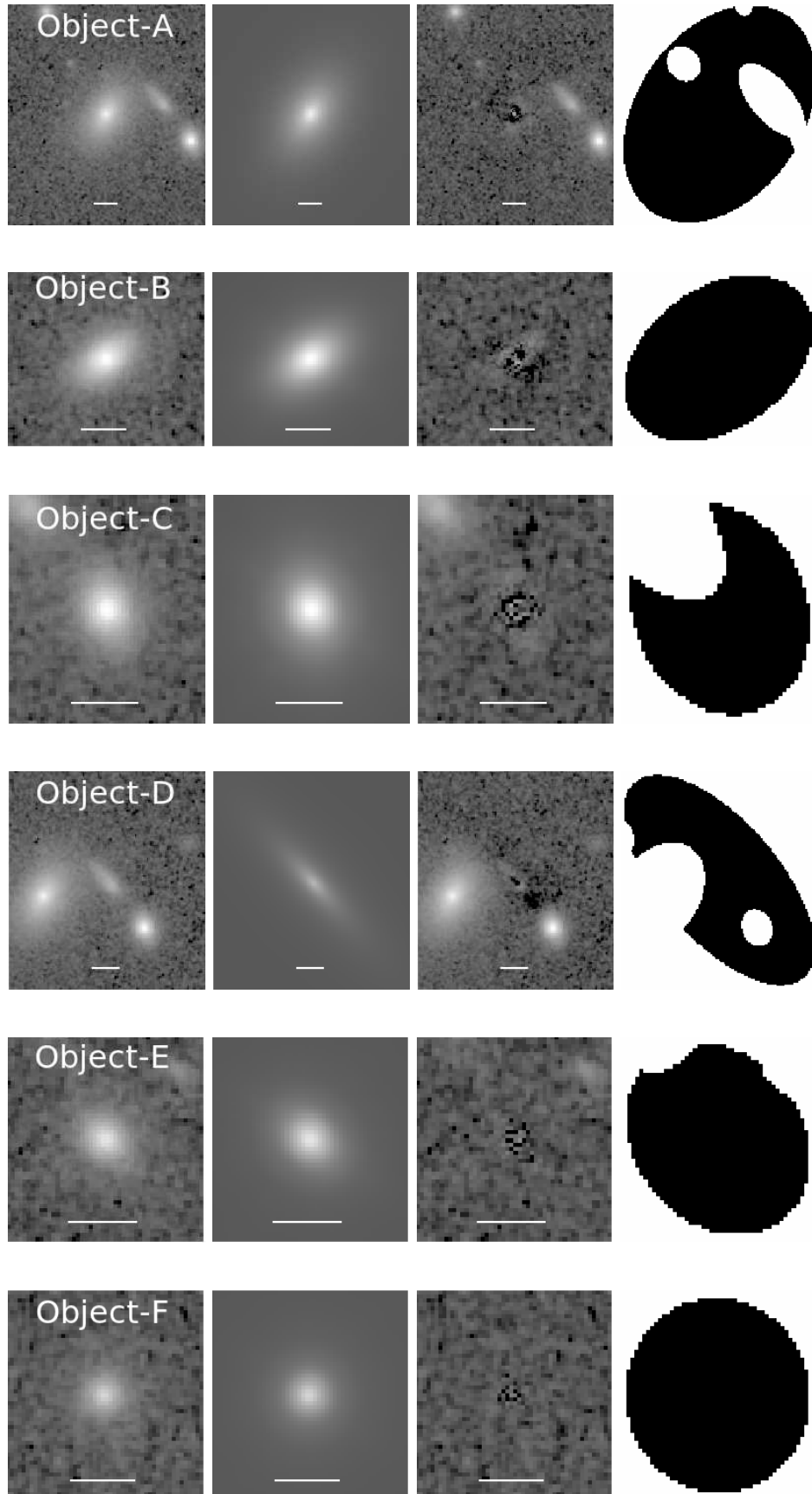


**Fig. 11.** In each plot, the panels show the input image, model galaxy, residual, and mask images from left to right. The plots are for object-A to F from top to bottom, respectively. The horizontal bar in each panel is 1 arcsec, which corresponds to 8.5 kpc (physical) at  $z = 1.6$ .

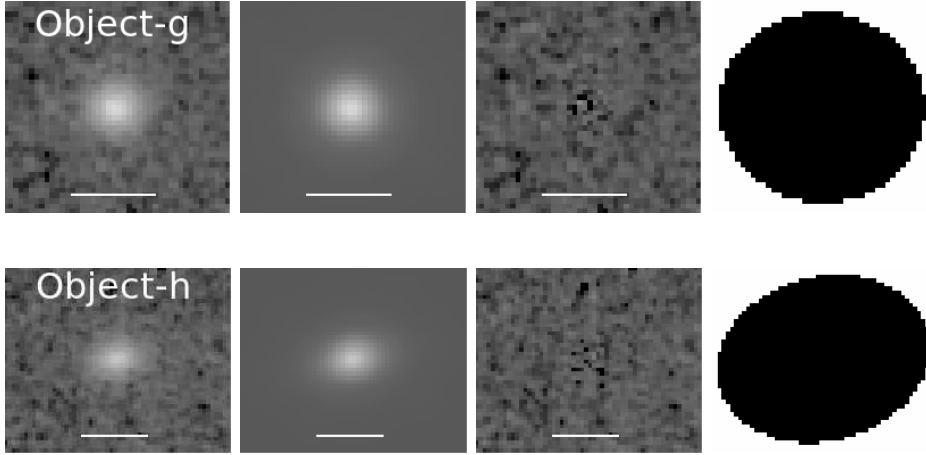


Fig. 12. As in Fig. 11, but for object-g and h.

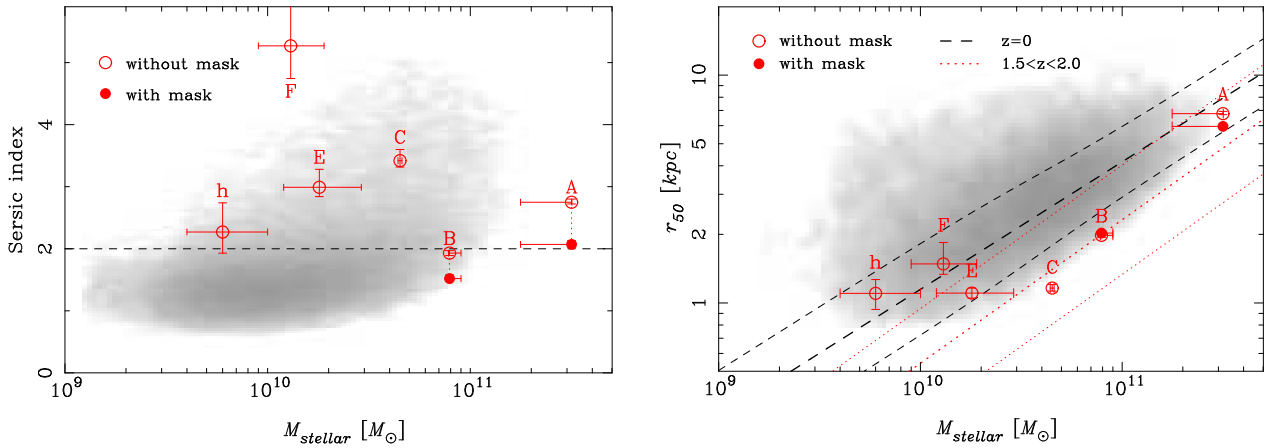


Fig. 13. **Left:** Sérsic index plotted against stellar mass. The gray scales are galaxies at  $0.05 < z < 0.07$  from SDSS. For clarify, only 95% of the galaxies are plotted. The large symbols are the  $z = 1.6$  galaxies and the associated error bars show the statistical uncertainty. We recall that we have a  $\sim 10\%$  systematic uncertainty on the structural parameters. Object-A and B likely host AGNs and we show the Sérsic index measured both with and without the central mask. Object-g is a moderately strong AGN and is not plotted here because no reliable stellar mass estimate is available, while Object-D is not plotted because we fail to find an adequate fit to this object. The horizontal dashed line shows the rough separation between early-type and late-type galaxies. **Right:** Half-light radius plotted against stellar mass. As in the left panel, the gray scales are for  $z = 0$  galaxies, but here we show only early-type galaxies with  $n > 2$ . The thick dashed line is the size-mass relation of early-type galaxies at  $z = 0$  from Shen et al. (2003) and the thin dashes lines show  $1\sigma$  scatter. The thick dotted line is for  $1.5 < z < 2.0$  quiescent early-type galaxies from Newman et al. (2012) and the thin dotted lines show a  $1\sigma$  scatter in the relation.

**Table 4.** Structural properties of galaxies. The numbers in the brackets are obtained by applying a circular mask of 3 pixel radius at the center (i.e.,  $\sim 2 \times \text{FWHM}$  region is masked) to avoid contamination of central point sources. Note that object-D is too close to the BGG and we fail to fit the object. Note as well that the uncertainties quoted here are statistical uncertainties. We expect  $\sim 10\%$  systematics on all the parameters.

ID	Sérsic index	half-light radius (kpc)	axial ratio
object-A	$2.75^{+0.05}_{-0.01}$ ( $2.07^{+0.06}_{-0.01}$ )	$8.75^{+0.20}_{-0.04}$ ( $7.69^{+0.14}_{-0.03}$ )	$0.60^{+0.01}_{-0.01}$ ( $0.60^{+0.01}_{-0.01}$ )
object-B	$1.93^{+0.04}_{-0.01}$ ( $1.52^{+0.06}_{-0.01}$ )	$2.60^{+0.03}_{-0.01}$ ( $2.66^{+0.03}_{-0.01}$ )	$0.58^{+0.01}_{-0.01}$ ( $0.58^{+0.01}_{-0.01}$ )
object-C	$3.42^{+0.18}_{-0.04}$	$1.42^{+0.05}_{-0.01}$	$0.67^{+0.02}_{-0.01}$
object-D	3.43	21.82	0.28
object-E	$2.99^{+0.29}_{-0.06}$	$1.36^{+0.07}_{-0.01}$	$0.66^{+0.03}_{-0.01}$
object-F	$5.27^{+1.21}_{-0.23}$	$1.53^{+0.37}_{-0.05}$	$0.94^{+0.06}_{-0.01}$
object-g	$2.26^{+0.38}_{-0.07}$ ( $1.27^{+0.77}_{-0.12}$ )	$0.83^{+0.05}_{-0.01}$ ( $1.09^{+0.22}_{-0.05}$ )	$0.82^{+0.06}_{-0.01}$ ( $0.84^{+0.07}_{-0.01}$ )
object-h	$2.27^{+0.47}_{-0.07}$	$1.59^{+0.14}_{-0.03}$	$0.48^{+0.05}_{-0.01}$

depends on environment. Rettura et al. (2010) studied a cluster at  $z = 1.24$  and suggested that the cluster and field galaxies at the same redshift have similar sizes. The newly confirmed group is one of the highest redshift systems discovered so far where high quality WFC3 images are available, allowing us to investigate galaxy sizes in the group.

We show half-light radius,  $r_{50}$ , against stellar mass in the right panel of Fig. 13. As a  $z = 0$  reference, we show the size-mass distribution of local early-type ( $n > 2$ ) galaxies as well as a size-mass relation of the local early-type galaxies from Shen et al. (2003). We note that Shen et al. (2003) measured sizes in the  $z$ -band, while we use the  $r$ -band. Therefore, care needs to be taken when comparing these two samples. We also note that the resolution limit of the F160W image is  $r_{50} \sim 0.5$  kpc and thus all the  $z = 1.6$  galaxies plotted are well resolved. The Figure also shows the size-mass relation for quiescent galaxies from Newman et al. (2012). Their quiescent galaxies typically have early-type morphology with  $n \sim 3 - 4$  and their result is directly comparable to ours. They did not characterize the environment of the galaxies. However, most of the galaxies in their sample are likely field galaxies and we refer to their sample as a field sample.

The BGG is within the scatter of the local and  $1.5 < z < 2.0$  size-mass relations and it appears that the BGG in the  $z = 1.6$  group already has a similar size to local massive galaxies. The low-mass galaxies with  $\sim 10^{10} M_{\odot}$  are also consistent with both relations. Only object-B and C are clearly below the local relation, and they are consistent with the  $1.5 < z < 2.0$  field relation. Overall, the size-mass relation of the group galaxies seems to fall in between the  $1.5 < z < 2.0$  and  $z = 0$  relations. Papovich et al. (2011) claimed that galaxies in another  $z = 1.6$  group in SXDF exhibit smaller sizes at fixed stellar mass compared to the local galaxies, but they are larger than field galaxies at the same redshift. Our result in Fig. 13 may be consistent with their finding. Zirm et al. (2012) reported on a similar trend in a  $z = 2.16$  proto-cluster. However, the statistics in all these studies, including this paper, are not sufficient to allow a clear conclusion.

Lotz et al. (2011) reported on an elevated merger/interaction rate in the  $z = 1.62$  system in

SXDF. Only one of the 8 group member candidates (object-D) shows a highly distorted morphology and all the other galaxies have well-defined early-type morphologies. We also do not observe a strong elevated rate of nearby companions (see Fig. 11). We may tend to miss interacting galaxies due to possibly poor photo- $z$ 's for such objects. To be sure, we visually inspect all the bright galaxies with  $H < 24$  located within  $r_{200}$  without using photo- $z$ 's. Fore-/background galaxies with secure spec- $z$ 's are excluded from this exercise. We find 3 clear cases for disturbed morphology in addition to object-D. We have carefully examined the SEDs of the 3 objects and find that only one of them is marginally consistent with being at the group redshift. The other SEDs look normal and they are likely at  $z \sim 3$ . Although the statistics are very poor, it is unlikely that a large fraction of the group galaxies are undergoing interaction. The possible different trend between the two systems might be due to their different dynamical states. That is, the newly confirmed  $z = 1.61$  group in this paper is a more relaxed system than the one in SXDF. If the X-ray emission around object-A is partly due to a cool core, it lends support a relaxed system with no recent merger events. It would then not be a surprise that few group members are undergoing interactions with other galaxies. On the other hand, the group in SXDS shows a somewhat irregular distribution of the members and it potentially has a companion group (but see also the shallow Chandra observations by Pierre et al. 2011). The possibly different dynamical states could explain the different merger/interaction rates in these two groups at the same redshift.

Finally, we briefly mention the ellipticity of the  $z = 1.6$  galaxies. As shown in Table 4, most of them have an axis ratio of  $b/a \sim 0.6$ . By excluding object-D, which we fail to fit, we measure an average axis ratio of 0.68 with a scatter of  $\sigma = 0.14$ . This axis ratio is consistent with field galaxies at similar redshifts ( $\langle b/a \rangle = 0.66$ ; Newman et al. 2012). Holden et al. (2009) found that cluster early-type galaxies have the median axis ratio of 0.70 and this does not strongly evolve at  $z < 1$ . Our finding here may extend the result by Holden et al. (2009) to a redshift of  $z = 1.6$ , although the cluster mass ranges explored are very

different (our group has a much lower mass than those studied by Holden et al. 2009).

To summarize, we find that most of the galaxies in the  $z = 1.6$  group are early-type galaxies with Sérsic index  $n > 2$ . There are a few galaxies that have smaller physical sizes than their local counterparts, but the overall size-mass relation of the group galaxies does not seem to be significantly different from the local relation. In all of these aspects, the group is strikingly similar to local groups and clusters and the environmental dependence of galaxy properties is clearly in place by  $z = 1.6$ .

## 6. Discussion

Our primary finding in this work is that the newly discovered, poor group of galaxies at  $z = 1.61$  in the CDFS is dominated by quiescent early-type galaxies. This result is possible because of the exquisite, high quality data available in this field. We started this paper by saying that high- $z$  groups hold a key to understanding the origin of the environmental dependence of galaxy properties observed locally because they are the progenitors of present-day clusters. The galaxy populations in the group appear strikingly similar to those in groups in the local universe. A naive interpretation of our results is that the environmental dependence is established at  $z \gg 1.6$ . In fact, Tanaka et al. (2010) found tentative evidence that a fraction of galaxies in a (proto-)cluster at  $z = 2.15$  show suppressed star formation activities. Spitler et al. (2011) reported on galaxy concentrations at  $z = 2.2$  in the COSMOS field and suggested that a red sequence is present, which might support the view of an environmental dependence already in place by  $z > 1.6$ .

Groups and clusters form from statistical fluctuations of the density field and they are thus statistical objects in nature. They do not all form at the same time and they do not all evolve in the same way. At a given redshift, groups naturally show a diversity in their properties and we cannot generalize our results in this paper to the average group properties at  $z = 1.6$ . However, it is still important that we find one system that is dominated by quiescent early-type galaxies. The environmental dependence of galaxy properties is thought to be due to both nature and nurture effects. Most of the group member candidates are consistent with the formation redshift of  $z_f = 3$ , which is only  $\sim 2$  Gyr prior to  $z = 1.6$  under the assumption of a single burst model (see Fig. 6). Given that galaxies need time (of order hundred Myr) to settle onto the red sequence even after a sharp quenching, the galaxies must have grown to  $10^{10-11} M_\odot$  and then quenched on a time scale of  $< 2$  Gyr. What physical process is responsible for such rapid evolution in this low mass group at this high redshift?

The  $z = 1.6$  group shows one significant difference from local groups and clusters; the high AGN fraction. Recently, energy feedback from AGNs has been suggested as a promising quenching mechanism. Theoretical work based on a simplified recipe of AGN energy feedback seems to do a good job of reproducing some observed

galaxy properties (e.g., Granato et al. 2004; Springel et al. 2005; Bower et al. 2006; Croton et al. 2006), although the exact form of the energy feedback is still highly uncertain. Our finding that the group hosts a large fraction of AGNs might indicate some role of AGN feedback in quenching. A fraction of AGNs with  $L_X > 10^{42} \text{ erg s}^{-1}$  at  $1 < z < 2$  among galaxies with  $> 2 \times 10^{10} M_\odot$  is about 10-20% in the field (Xue et al. 2010). If we use object-A to E, which are  $> 2 \times 10^{10} M_\odot$  within the error, we find an AGN fraction of  $0.40^{+0.30}_{-0.25}$ . The fractions are consistent within the errors, but the large AGN fraction in groups is not unexpected based on the increasing AGN fraction with redshift in  $z < 1.3$  groups and clusters (Eastman et al. 2007; Martini et al. 2009; Tanaka et al. 2011). Even in a proto-cluster at a higher redshift of  $z = 3.1$ , Lehmer et al. (2009) observed an enhanced fraction of AGNs. However, an enhanced AGN fraction is only circumstantial hint – we do not observe any direct evidence that AGNs quench the galaxies.

Another interesting aspect of the high AGN fraction in high- $z$  groups is that it may help explain at least partly the apparent diversity of the observed properties of high- $z$  group galaxies. Tran et al. (2010) claimed that the SFR-density relation reverses in a group at  $z = 1.62$  in SXDF. We go comparably as deep as Tran et al. (2010) in this study, but we do not find the group as an active place for star formation (see Table 2). We do not observe an enhanced MIPS population in our group either. Not only the group studied by Tran et al. (2010), but another massive cluster at a similar redshift ( $z = 1.45$ ) seems to host a large population of emission line objects in the core (Hilton et al. 2010; Hayashi et al. 2010). It is still unclear whether these MIPS sources and emission line objects are due to enhanced star formation or AGN activity. The latter possibility is not unlikely given the recently observed high AGN fractions in high redshift groups and clusters as mentioned above and AGNs may contribute at least partly to the observed fraction of emission line galaxies.

AGN feedback is a possible process to quench galaxies, but are there any other physical processes that could explain the observed trend? Physical processes like ram-pressure stripping (Gunn & Gott 1972) and harassment (Moore et al. 1996) may not be very efficient in groups because these processes are expected to be effective in rich clusters. Strangulation (Larson et al. 1980) may work in groups, and it may be able to suppress the star formation on a short enough time scale to bring the galaxies onto the red sequence within  $< 2$  Gyr. Galaxy interactions and mergers may play some role in quenching as well, although we do not observe a hint of frequent interactions in the group. If interactions are important, they must have happened at higher redshifts, which would then be closely linked to the nature effects. The observed large fraction of AGNs makes us speculate their roles, but as discussed earlier, we do not have direct evidence for the AGN feedback. In order to further constrain the physical processes, it would be interesting to perform deep near-IR spectroscopy to measure the Balmer absorption features. These absorptions are strongest in A-type stars

and by combining them with a continuum shape (e.g., a strength of the 4000Å break), one can put a constraint on the quenching time scale, which will then constrain the physical processes.

Although the discovery of the high- $z$  poor group filled with quiescent early-type galaxies is interesting, we need a larger sample of groups at high redshifts to fully address the questions raised in the first section. We are now in the process of building such a statistical sample of high- $z$  groups. Up-coming large imaging surveys such as the one by Hyper Suprime-Cam will provide a huge data set that allows us to construct a statistical sample of high redshift groups and study the group evolution up to  $z = 2$  and beyond. If increasing AGN activity in high- $z$  groups is a real trend, it might imply that future deep X-ray surveys aiming at distant groups might benefit from moderately high angular resolution. The XMM-Newton data of the group appears dominated by a collection of point sources as one can easily imagine from the Chandra data shown in Fig. 1. We are able to subtract such contamination and detect the extended component in the XMM data (see Sect. 3.2), but the detection of extended X-ray is obviously harder where point source contamination is more severe. High angular resolution X-ray missions such as WFXT (Vikhlinin et al. 2009) and SMART-X would be ideal for identifying high redshift groups and clusters.

## 7. Conclusion

We have discovered a group of galaxies at  $z = 1.61$  in CDFS using the deep X-ray, optical, and near-IR data. This is the lowest mass system discovered so far at such high redshifts and it provides an interesting system to study galaxy evolution in groups at high redshift. Our primary findings can be summarized as follows.

- We detect extended X-ray emission from the group, which suggests that the group is gravitationally bound.
- The photo- $z$  selected galaxies at  $z = 1.6$  exhibit a clear concentration of red galaxies around the extended X-ray emission. A few of them, including the BGG, are spectroscopically confirmed at  $z \sim 1.61$ .
- The group members form a pronounced red sequence, and are mostly consistent with a simple model population formed at  $z_f = 3$ . We fit our SEDs with models assuming stellar populations are formed with exponentially declining star formation histories. The best fits suggest that stellar populations are predominantly old and passively evolving, with low star formation rates,  $\text{SFR} \ll 1 M_\odot \text{ yr}^{-1}$ . Our galaxies lie clearly below the SFR-mass relation for normal star forming galaxies at similar redshifts.
- We have performed a morphological analysis using the WFC3 data and found that most of the group members show early-type morphology with Sérsic index  $n > 2$ .
- Although the statistics are poor, the group appears to exhibit a very high fraction of AGNs (3 out of

8 good/likely candidates are AGNs), indicating an elevated AGN activity in high redshift groups.

These findings lead us to conclude that quiescent, early-type galaxies have already become a dominant population in the group. The group thus appears similar to present-day groups and clusters with one possible difference of its high AGN fraction. This is a surprising result given the very low-mass of the system and its very high redshift. A naive interpretation of our result is that the environmental dependence of galaxy properties is in place in this group and it must have come in place at  $z > 1.6$ . However, the physical process or processes responsible for the galaxy quenching remain unclear. Furthermore, there appears to be significant diversity in the observed properties of group/cluster galaxies at  $z \gtrsim 1.5$ . To better understand high redshift groups, statistical samples will be necessary. Future surveys will yield such samples which will hopefully allow us to address the long standing issue of the interplay between structure evolution and galaxy evolution.

We thank the anonymous referees for useful comments, which helped improve the paper. This work was supported by World Premier International Research Center Initiative (WPI Initiative), MEXT, Japan, by KAKENHI No. 23740144, and by SAO grants SP1-12006B and SP8-9003C to UMBC. WNB and YQX acknowledge support from Chandra grant SP1-12007A and JSM acknowledges support from Chandra grant SP1-12006A. YQX also acknowledges support from the Youth 1000 Plan (QingNianQianRen) program and the USTC startup funding. This work is based on observations taken by the CANDELS Multi-Cycle Treasury Program with the NASA/ESA HST, which is operated by the Association of Universities for Research in Astronomy, Inc., under NASA contract NAS5-26555. Funding for the SDSS and SDSS-II has been provided by the Alfred P. Sloan Foundation, the Participating Institutions, the National Science Foundation, the U.S. Department of Energy, the National Aeronautics and Space Administration, the Japanese Monbukagakusho, the Max Planck Society, and the Higher Education Funding Council for England. The SDSS Web Site is <http://www.sdss.org/>.

## Appendix 1. Foreground over-density at $z = 1$

There are three objects at  $z_{spec} = 1$  within the X-ray contours in Fig. 1. In this appendix, we argue that they are not the primary counterpart of the X-ray emission.

In Fig. 14, we show  $r - z$  color against  $z$ -band magnitude of galaxies at  $z \sim 1$  around the extended X-ray emission. Most of the galaxies are blue and there is only a weak red sequence. In fact, our red sequence finder described in Section 2.3 gives a signal of only  $0.6\sigma$  at  $z = 1$ . As shown in Fig. 6, the red sequence is clearly more pronounced at  $z = 1.6$ . Furthermore, the brightest galaxy at  $z_{spec} = 1.03$  is 1 mag. fainter than  $m^*$  and there is no  $m^*$  galaxy around the X-ray emission at  $z_{phot} = 1$ . The lack of bright galaxies does not favor the interpretation that

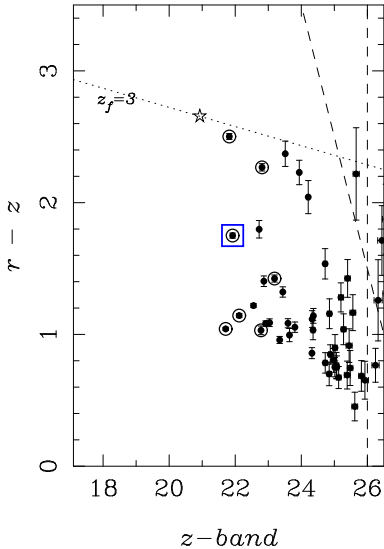


**Fig. 14.** F606W-LP850 plotted against LP850 using the MUSIC catalog. Here, we denote F606W and LP850 filters as  $r$  and  $z$ , respectively. The large points are galaxies with  $P_{gr, z_{gr}=1.03} > 0.16$  within  $r_{200}$  of the group. The double-circles are spectroscopic galaxies at  $|z_{spec} - 1.03| < 0.02$  and the square shows an X-ray point source. The slanted dotted line is a model red sequence at  $z = 1.03$  formed at  $z_f = 3$  and the star indicates  $m_z^*$ . The dashed lines are  $5\sigma$  limits.

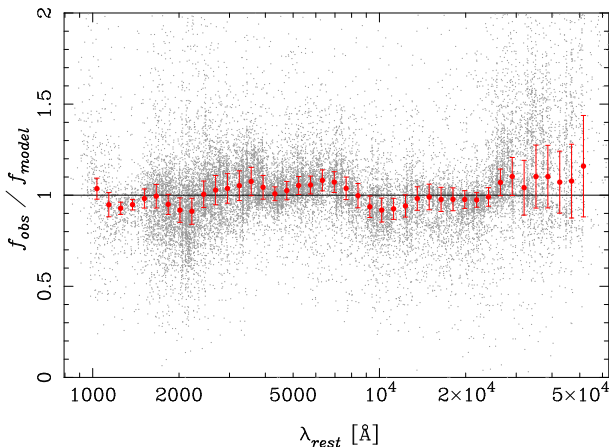


**Fig. 15.** Observed to model flux ratio is plotted against rest-frame wavelength. The dots are each photometry and the big points show the median of the ratio in each wavelength bin. The associated error bars show the  $1\sigma$  error range after subtracting the photometric uncertainty in the quadrature.

they form an X-ray bright group. Although we cannot completely reject the possibility of the  $z \sim 1$  galaxies contributing to the extended X-ray emission, they are highly unlikely the primary counterpart of the X-ray.

## Appendix 2. Template error function for SED fitting

Model templates based on a stellar population synthesis code are subject to systematic uncertainties. Such un-

certainties include flux errors in the input stellar spectra used in a code and errors in the stellar evolutionary track. These systematics cause a mismatch between model spectra and observed spectra of galaxies. A way to crudely reduce such systematics is to apply flux corrections to model templates as a function of rest-frame wavelength. In principle, one could apply such correction to templates of a given spectral type. However, degeneracies between model parameters and a limited number of high quality spectra covering a wide enough wavelength window are major obstacles. One could instead apply a single ‘master’ correction to all the templates to crudely correct for the systematics. Here we construct a master *template error function* using the photometry of spectroscopically observed objects in CDFS and apply the error function to all the templates used in the SED fits. As noted in the main body of the paper, our conclusions do not change at all if we do not include the template error function in our analysis.

We first select galaxies with secure spectroscopic redshifts from the public spectroscopic redshift catalogs in the literature. We then fit SEDs of these galaxies with redshifts fixed to their spectroscopic redshifts using the photometry from the MUSIC catalog. The dots in Fig. 15 show the ratio between observed fluxes and best-fit model templates. The large points are the median of the ratio in each wavelength bin and the associated error bars are the  $1\sigma$  scatter in the ratio after subtracting the photometric error. The template error function defined here is a set of two quantities: the flux stretch and dispersion. We use both information in the SED fitting performed in the main body of the paper. We first apply flux stretches to the model templates and then take into account uncertainties in model fluxes in a given band in the fits. The latter procedure is important as pointed out by Brammer et al. (2008) because the accuracy of model templates is dependent on wavelength. Our model templates are most reliable (i.e., the dispersion is smallest) in the rest-frame optical, where population synthesis models are calibrated to real data. They become less reliable at shorter and longer wavelengths. SED fits can be improved by taking such model uncertainties into account.

The template flux uncertainties can be larger than photometric uncertainties especially for bright objects and this makes a fit too good – reduced  $\chi^2$  of a fit for a bright object is typically below 1. This does not mean that observed photometry has pessimistic errors, but it simply means that model templates are uncertain. In fact, the template error function increases the error ranges of all the physical parameters such as SFR and stellar mass, but the increased uncertainties likely represent more realistic uncertainties on the physical parameters. Note that the template error function does not completely remove the systematics. For example, as mentioned in the main body of the paper, we assume  $\tau$ -models, but no real galaxies would exactly follow the exponential decay. We force them to fit with  $\tau$ -models, which introduces systematic uncertainties. There is no straightforward way to quantify such systematics and it remains one of the major uncer-

tainties in our analysis.

## References

- Andreon, S., Maughan, B., Trinchieri, G., & Kurk, J. 2009, *A&A*, 507, 147
- Balestra, I., Mainieri, V., Popesso, P., et al. 2010, *A&A*, 512, A12
- Balogh, M., McGee, S., Wilman, D., Bower, et al. 2009, *MNRAS*, 398, 754
- Bauer, A. E., Grützbauch, R., Jørgensen, I., Varela, J., & Bergmann, M. 2011, *MNRAS*, 411, 2009
- Bertin, E., & Arnouts, S. 1996, *A&AS*, 117, 393
- Bielby, R. M., Finoguenov, A., Tanaka, M., et al. 2010, *A&A*, 523, A66
- Blanton, M. R., Schlegel, D. J., Strauss, M. A., et al. 2005, *AJ*, 129, 2562
- Bower, R. G., Benson, A. J., Malbon, R., Helly, J. C., Frenk, C. S., Baugh, C. M., Cole, S., & Lacey, C. G. 2006, *MNRAS*, 370, 645
- Brammer, G. B., van Dokkum, P. G., & Coppi, P. 2008, *ApJ*, 686, 1503
- Brodwin, M., Stern, D., Vikhlinin, A., et al. 2011, *ApJ*, 732, 33
- Bruzual, G., & Charlot, S. 2003, *MNRAS*, 344, 1000
- Calzetti, D., Armus, L., Bohlin, R. C., et al. 2000, *ApJ*, 533, 682
- Cardamone, C. N., van Dokkum, P. G., Urry, C. M., et al. 2010, *ApJS*, 189, 270
- Chabrier, G. 2003, *PASP*, 115, 763
- Cimatti, A., Pozzetti, L., Mignoli, M., et al. 2002, *A&A*, 391, L1
- Cooper, M. C., Yan, R., Dickinson, M., et al. 2011, *arXiv:1112.0312*
- Comastri, A., Ranalli, P., Iwasawa, K., et al. 2011, *A&A*, 526, L9
- Cristiani, S., Appenzeller, I., Arnouts, S., et al. 2000, *A&A*, 359, 489
- Croom, S. M., Warren, S. J., & Glazebrook, K. 2001, *MNRAS*, 328, 150
- Croton, D. J., et al. 2006, *MNRAS*, 365, 11
- Daddi, E., Renzini, A., Pirzkal, N., et al. 2005, *ApJ*, 626, 680
- Damen, M., Labbé, I., van Dokkum, P. G., et al. 2011, *ApJ*, 727, 1
- Doi, M., Tanaka, M., Fukugita, M., et al. 2010, *AJ*, 139, 1628
- Doherty, M., Bunker, A. J., Ellis, R. S., & McCarthy, P. J. 2005, *MNRAS*, 361, 525
- Dressler, A. 1980, *ApJ*, 236, 351
- Eastman, J., Martini, P., Sivakoff, G., et al. 2007, *ApJL*, 664, L9
- Elbaz, D., Daddi, E., Le Borgne, D., et al. 2007, *A&A*, 468, 33
- Fassbender, R., Nastasi, A., Böhringer, H., et al. 2011, *A&A*, 527, L10
- Fassbender, R., Suhada, R., & Nastasi, A. 2012, *arXiv:1203.5337*
- Feldmann, R., Carollo, C. M., Porciani, C., et al. 2006, *MNRAS*, 372, 565
- Finoguenov, A., Guzzo, L., Hasinger, G., et al. 2007, *ApJS*, 172, 182
- Finoguenov, A., Connelly, J. L., Parker, L. C., et al. 2009, *ApJ*, 704, 564
- Finoguenov, A., Watson, M. G., Tanaka, M., et al. 2010, *MNRAS*, 403, 2063
- Gawiser, E., van Dokkum, P. G., Herrera, D., et al. 2006, *ApJS*, 162, 1
- Giacconi, R., Zirm, A., Wang, J., et al. 2002, *ApJS*, 139, 369
- Giodini, S., Pierini, D., Finoguenov, A., et al. 2009, *ApJ*, 703, 982
- Gobat, R., Daddi, E., Onodera, M., et al. 2011, *A&A*, 526, A133
- Granato, G. L., De Zotti, G., Silva, L., Bressan, A., & Danese, L. 2004, *ApJ*, 600, 580
- Grazian, A., Fontana, A., de Santis, C., et al. 2006, *A&A*, 449, 951
- Grogin, N. A., Kocevski, D. D., Faber, S. M., et al. 2011, *arXiv:1105.3753*
- Gunn, J. E., & Gott, J. R., III 1972, *ApJ*, 176, 1
- Henry, J. P., Salvato, M., Finoguenov, A., et al. 2010, *ApJ*, 725, 615
- Hayashi, M., Kodama, T., Koyama, Y., et al. 2010, *MNRAS*, 402, 1980
- Hickox, R. C., & Markevitch, M. 2006, *ApJ*, 645, 95
- Hilton, M., Collins, C. A., Stanford, S. A., et al. 2007, *ApJ*, 670, 1000
- Hilton, M., Lloyd-Davies, E., Stanford, S. A., et al. 2010, *ApJ*, 718, 133
- Holden, B. P., Franx, M., Illingworth, G. D., et al. 2009, *ApJ*, 693, 617
- Jee, M. J., Rosati, P., Ford, H. C., et al. 2009, *ApJ*, 704, 672
- Jelic, V., Smolcic, V., Finoguenov, A., et al. 2012, *arXiv:1204.2552*
- Kennicutt, R. C., Jr. 1998, *ARA&A*, 36, 189
- Koekemoer, A. M., Faber, S. M., Ferguson, H. C., et al. 2011, *arXiv:1105.3754*
- Kodama, T., & Arimoto, N. 1997, *A&A*, 320, 41
- Kurk, J. D., Cimatti, A., di Serego Alighieri, S., et al. 2004, *A&A*, 422, L13
- Kurk, J., Cimatti, A., Zamorani, G., et al. 2009, *A&A*, 504, 331
- Larson, R. B., Tinsley, B. M., & Caldwell, C. N. 1980, *ApJ*, 237, 692
- Leauthaud, A., Finoguenov, A., Kneib, J.-P., et al. 2010, *ApJ*, 709, 97
- Leauthaud, A., Tinker, J., Bundy, K., et al. 2012, *ApJ*, 744, 159
- Le Fèvre, O., Vettolani, G., Garilli, B., et al. 2005, *A&A*, 439, 845
- Lehmer, B. D., Brandt, W. N., Alexander, D. M., et al. 2005, *ApJS*, 161, 21
- Lehmer, B. D., Alexander, D. M., Geach, J. E., et al. 2009, *ApJ*, 691, 687
- Lidman, C., Rosati, P., Tanaka, M., et al. 2008, *A&A*, 489, 981
- Lotz, J. M., Papovich, C., Faber, S. M., et al. 2011, *arXiv:1110.3821*
- Luo, B., Bauer, F. E., Brandt, W. N., et al. 2008, *ApJS*, 179, 19
- Luo, B., Brandt, W. N., Xue, Y. Q., et al. 2010, *ApJS*, 187, 560
- Martini, P., Sivakoff, G. R., & Mulchaey, J. S. 2009, *ApJ*, 701, 66
- Maraston, C., Pforr, J., Renzini, A., et al. 2010, *MNRAS*, 407, 830
- Martini, P., Mulchaey, J. S., & Kelson, D. D. 2007, *ApJ*, 664, 761
- Matsuda, Y., Yamada, T., Hayashino, T., et al. 2004, *AJ*, 128, 569

- Mignoli, M., Cimatti, A., Zamorani, G., et al. 2005, *A&A*, 437, 883
- Miley, G., & De Breuck, C. 2008, *A&A Rev.*, 15, 67
- Miller, N. A., Fomalont, E. B., Kellermann, K. I., et al. 2008, *ApJS*, 179, 114
- Moore, B., Katz, N., Lake, G., Dressler, A., & Oemler, A. 1996, *Nature*, 379, 613
- Mullis, C. R., Rosati, P., Lamer, G., et al. 2005, *ApJL*, 623, L85
- Nastasi, A., Fassbender, R., Böhringer, H., et al. 2011, *A&A*, 532, L6
- Newman, A. B., Ellis, R. S., Bundy, K., & Treu, T. 2012, *ApJ*, 746, 162
- Nonino, M., Dickinson, M., Rosati, P., et al. 2009, *ApJS*, 183, 244
- Noeske, K. G., Weiner, B. J., Faber, S. M., et al. 2007, *ApJL*, 660, L43
- Pacifici, C., Charlot, S., Blaizot, J., & Brinchmann, J. 2012, *MNRAS*, 421, 2002
- Papovich, C., Momcheva, I., Willmer, C. N. A., et al. 2010, *ApJ*, 716, 1503
- Papovich, C., Bassett, R., Lotz, J. M., et al. 2011, arXiv:1110.3794
- Peng, C. Y., Ho, L. C., Impey, C. D., & Rix, H.-W. 2002, *AJ*, 124, 266
- Peng, C. Y., Ho, L. C., Impey, C. D., & Rix, H.-W. 2010, *AJ*, 139, 2097
- Pierre, M., Clerc, N., Maughan, B., et al. 2011, arXiv:1109.6194
- Polletta, M., Tajer, M., Maraschi, L., et al. 2007, *ApJ*, 663, 81
- Popesso, P., Dickinson, M., Nonino, M., et al. 2009, *A&A*, 494, 443
- Popesso, P., Biviano, A., Rodighiero, G., et al. 2012, *A&A*, 537, A58
- Postman, M., & Geller, M. J. 1984, *ApJ*, 281, 95
- Quadri, R. F., Williams, R. J., Franx, M., & Hildebrandt, H. 2012, *ApJ*, 744, 88
- Rafferty, D. A., Brandt, W. N., Alexander, D. M., et al. 2011, *ApJ*, 742, 3
- Ravikumar, C. D., Puech, M., Flores, H., et al. 2007, *A&A*, 465, 1099
- Reddy, N. A., Steidel, C. C., Fadda, D., et al. 2006, *ApJ*, 644, 792
- Rettura, A., Rosati, P., Nonino, M., et al. 2010, *ApJ*, 709, 512
- Santini, P., Fontana, A., Grazian, A., et al. 2009, *A&A*, 504, 751
- Santos, J. S., Fassbender, R., Nastasi, A., et al. 2011, *A&A*, 531, L15
- Shen, S., Mo, H. J., White, S. D. M., et al. 2003, *MNRAS*, 343, 978
- Spitler, L. R., Labbé, I., Glazebrook, K., et al. 2011, arXiv:1112.2691
- Springel, V., Di Matteo, T., & Hernquist, L. 2005, *MNRAS*, 361, 776
- Stanford, S. A., Eisenhardt, P. R., Brodwin, M., et al. 2005, *ApJL*, 634, L129
- Stanford, S. A., Romer, A. K., Sabirli, K., et al. 2006, *ApJL*, 646, L13
- Stanford, S. A., Brodwin, M., Gonzalez, A. H., et al. 2012, arXiv:1205.3786
- Strauss, M. A., Weinberg, D. H., Lupton, R. H., et al. 2002, *AJ*, 124, 1810
- Strolger, L.-G., Riess, A. G., Dahlen, T., et al. 2004, *ApJ*, 613, 200
- Szokoly, G. P., Bergeron, J., Hasinger, G., et al. 2004, *ApJS*, 155, 271
- Tanaka, M., Kodama, T., Arimoto, N., et al. 2005, *MNRAS*, 362, 268
- Tanaka, M., Kodama, T., Kajisawa, M., et al. 2007, *MNRAS*, 377, 1206
- Tanaka, M., Finoguenov, A., & Ueda, Y. 2010a, *ApJL*, 716, L152
- Tanaka, M., De Breuck, C., Venemans, B., & Kurk, J. 2010b, *A&A*, 518, A18
- Tanaka, M., Finoguenov, A., Lilly, S. J., et al. 2011, arXiv:1110.0979
- Tanaka, M. 2011a, arXiv:1111.0132
- Tanaka, M. 2011b, arXiv:1111.0133
- Taylor, E. N., Franx, M., van Dokkum, P. G., et al. 2009, *ApJS*, 183, 295
- Toft, S., van Dokkum, P., Franx, M., et al. 2007, *ApJ*, 671, 285
- Tran, K.-V. H., Papovich, C., Saintonge, A., et al. 2010, *ApJL*, 719, L126
- Trujillo, I., Förster Schreiber, N. M., Rudnick, G., et al. 2006, *ApJ*, 650, 18
- York, D. G., Adelman, J., Anderson, J. E., Jr., et al. 2000, *AJ*, 120, 1579
- van der Wel, A., Franx, M., van Dokkum, P. G., & Rix, H.-W. 2004, *ApJL*, 601, L5
- Vanzella, E., Cristiani, S., Dickinson, M., et al. 2008, *A&A*, 478, 83
- Venemans, B. P., Kurk, J. D., Miley, G. K., et al. 2002, *ApJL*, 569, L11
- Venemans, B. P., Röttgering, H. J. A., Miley, G. K., et al. 2007, *A&A*, 461, 823
- Vikhlinin, A., Murray, S., Gilli, R., et al. 2009, *astro2010: The Astronomy and Astrophysics Decadal Survey*, 2010, 305
- Williams, R. J., Quadri, R. F., Franx, M., van Dokkum, P., & Labbé, I. 2009, *ApJ*, 691, 1879
- Wolf, C., Meisenheimer, K., Kleinheinrich, M., et al. 2004, *A&A*, 421, 913
- Wolf, C., Hildebrandt, H., Taylor, E. N., & Meisenheimer, K. 2008, *A&A*, 492, 933
- Wuyts, S., Förster Schreiber, N. M., van der Wel, A., et al. 2011, *ApJ*, 742, 96
- Xue, Y. Q., Brandt, W. N., Luo, B., et al. 2010, *ApJ*, 720, 368
- Xue, Y. Q., Luo, B., Brandt, W. N., et al. 2011, *ApJS*, 195, 10
- Zirm, A. W., Toft, S., & Tanaka, M. 2012, *ApJ*, 744, 181